The Astronomical Journal, 166:113 (23pp), 2023 September https://doi.org/10.3847/1538-3881/aceb5a
© 2023. The Author(s). Published by the American Astronomical Society.
OPEN ACCESS

A Search for Gas-Rich Dwarf Galaxies in the Local Universe with ALFALFA and the WIYN One Degree Imager

Katherine L. Rhode[1], Nicholas J. Smith[1], William F. Janesh[2], John J. Salzer[1], Elizabeth A. K. Adams[3,4], Martha P. Haynes[5], Steven Janowiecki[6], and John M. Cannon[7]
[1] Department of Astronomy, Indiana University, 727 East Third Street, Bloomington, IN 47405, USA; krhode@indiana.edu
[2] Department of Astronomy, Case Western Reserve University, 10900 Euclid Avenue, Cleveland, OH 44106, USA
[3] ASTRON, Netherlands Institute for Radio Astronomy, Oude Hoogeveensedijk 4, 7991 PD Dwingeloo, The Netherlands
[4] Kapteyn Astronomical Institute, University of Groningen, Landleven 12, 9747 AD, Groningen, The Netherlands
[5] Cornell Center for Astrophysics and Planetary Science, Space Sciences Building, Cornell University, Ithaca, NY 14853, USA
[6] University of Texas, Hobby–Eberly Telescope, McDonald Observatory, TX 79734, USA
[7] Department of Physics & Astronomy, Macalester College, 1600 Grand Avenue, Saint Paul, MN 55105, USA
Received 2023 June 14; revised 2023 July 26; accepted 2023 July 26; published 2023 August 18

Abstract

We present results from an optical search for Local Group dwarf galaxy candidates associated with the Ultra-Compact High Velocity Clouds (UCHVCs) discovered by the ALFALFA neutral hydrogen survey. The ALFALFA UCHVCs are isolated, compact H I clouds with projected sizes, velocities, and estimated H I masses that suggest they may be nearby dwarf galaxies, but that have no clear counterpart in existing optical survey data. We observed 26 UCHVCs with the WIYN 3.5 m telescope and One Degree Imager (ODI) in two broadband filters and searched the images for resolved stars with properties that match those of stars in typical dwarf galaxies at distances <2.5 Mpc. We identify one promising dwarf galaxy candidate at a distance of ∼570 kpc associated with the UCHVC AGC 268071, and five other candidates that may deserve additional follow-up. We carry out a detailed analysis of ODI imaging of a UCHVC that is close in both projected distance and radial velocity to the outer-halo Milky Way globular cluster Pal 3. We also use our improved detection methods to reanalyze images of five UCHVCs that were found to have possible optical counterparts during the first phase of the project, and confirm the detection of a possible stellar counterpart to the UCHVC AGC 249525 at an estimated distance of ∼2 Mpc. We compare the optical and H I properties of the dwarf galaxy candidates to the results from recent theoretical simulations that model satellite galaxy populations in group environments, as well as to the observed properties of galaxies in and around the Local Group.

Unified Astronomy Thesaurus concepts: Dwarf galaxies (416); Local Group (929); Neutral hydrogen clouds (1099); Sloan photometry (1465); Optical observation (1169); Extragalactic radio sources (508); Stellar photometry (1620)

1. Introduction

The Arecibo Legacy Fast ALFA survey (ALFALFA; Giovanelli et al. 2005; Haynes et al. 2018) was a survey for H I emission carried out from 2005−2012 with the Arecibo *L*-band Feed Array (ALFA) instrument on the 305 m Arecibo radio telescope. The survey covered ∼7000 sq. degrees of sky in drift-scan mode, detecting sources of 21 cm line emission without regard to the locations of optical sources. The final catalog produced by the ALFALFA survey includes ∼31,500 H I sources out to a redshift of $z \sim 0.06$, a large fraction of which had never before been observed via their 21 cm emission (Haynes et al. 2018).

Because of its excellent sensitivity, ALFALFA was able to detect objects with only modest amounts of H I ($\sim 10^4$–$10^5\ M_\odot$) out to distances beyond the edge of the Local Group. A new class of potentially nearby, low-mass H I sources was identified in the ALFALFA survey data and dubbed Ultra-Compact High Velocity Clouds (UCHVCs; Giovanelli et al. 2010). Roughly 100 of these objects were found in ALFALFA; Adams et al. (2013) laid out a set of criteria for sources that qualify as UCHVCs and presented an initial catalog. These objects are compact (angular diameter <30′), low-mass (H I masses of 10^5–$10^6\ M_\odot$ at 1 Mpc), isolated from other sources in terms of both sky position and velocity, and have velocities that help distinguish them from Galactic high-velocity clouds (HVCs) while making them likely to be located within the Local Volume. Perhaps most importantly, ALFALFA sources are classified as UCHVCs only if they lack an obvious optical counterpart when matched with existing optical survey data from the Sloan Digital Sky Survey (SDSS; York et al. 2000; Eisenstein et al. 2011) or the Digitized Sky Survey (DSS).

The properties of the UCHVCs imply that these objects could represent a population of low-mass, gas-bearing dark matter halos located in and around the Local Group; this is the "minihalo hypothesis" described in Giovanelli et al. (2010) and Adams et al. (2013). Accordingly, our group has been observing a selection of the UCHVCs at optical wavelengths in order to investigate their nature and the possibility that the UCHVCs are nearby gas-rich dwarf galaxies that have previously gone undetected. We image the UCHVC locations at optical wavelengths with the WIYN 3.5 m Observatory[8] and systematically search the area around the location of the H I

Original content from this work may be used under the terms of the Creative Commons Attribution 4.0 licence. Any further distribution of this work must maintain attribution to the author(s) and the title of the work, journal citation and DOI.

[8] The WIYN Observatory is a joint facility of the NSFs National Optical-Infrared Astronomy Research Laboratory, Indiana University, the University of Wisconsin–Madison, Pennsylvania State University, and Purdue University.

detection to identify any stellar populations that may be associated with the neutral gas. The first UCHVC we observed with WIYN led to the discovery of the nearby gas-rich dwarf galaxy Leo P (Giovanelli et al. 2013; Rhode et al. 2013), which is located just outside the Local Group at ∼1.6 Mpc, is extremely metal-deficient, and is the lowest-mass galaxy known that is actively forming stars (Skillman et al. 2013; McQuinn et al. 2015).

After the discovery of Leo P, we initiated a systematic optical observing campaign that targeted UCHVCs from the catalog presented in Adams et al. (2013) as well as additional sources drawn from the low-velocity ALFALFA grids. We used wide-field imaging in two broadband filters, resolved stellar photometry, and a color–magnitude diagram (CMD) filtering technique to search for the presence of possible stellar populations associated with the H I clouds over a distance range of 250 kpc to 2.5 Mpc. The first part of the campaign was carried out with the WIYN One Degree Imager (ODI) with a partially filled focal plane—an instrument referred to as pODI—and focused mainly on objects with higher H I column density values. In addition, it used the Very Large Array (VLA) and the Westerbork Synthesis Radio Telescope (WSRT) to acquire and analyze H I synthesis data for several of the targets in the pODI sample, in order to obtain more detailed information about the objects' H I distributions and kinematics (e.g., Adams et al. 2016, 2015; Bralts-Kelly et al. 2020; Paine et al. 2020). Optical imaging studies were also carried out by other groups to search for counterparts to the UCHVCs and to other potentially nearby gas-rich sources found in surveys like GALFA-HI (Bellazzini et al. 2015a, 2015b; Sand et al. 2015); the results from these studies will be discussed further in later sections of this paper.

A total of 23 UCHVCs that were observed with WIYN pODI were analyzed in the first phase of the project. In Janesh et al. (2015), we described the WIYN survey and methods and presented some initial results for AGC 198606, a UCHVC that is close in both projected spatial location and velocity to the Local Group dwarf galaxy Leo T (Irwin et al. 2007; Ryan-Weber et al. 2008). Results for another UCHVC, AGC 249525, were initially presented in Janesh et al. (2017), and the complete set of results for the first 23 UCHVCs we analyzed was published in Janesh et al. (2019, hereafter J19). J19 identified a total of five UCHVCs that had possible faint stellar counterparts in the pODI imaging data. These five counterparts had estimated distances ranging from ∼350 kpc to 1.6 Mpc and estimated total optical magnitudes between $M_V = -1.4$ and -7.1 mag.

The second phase of our UCHVC follow-up imaging campaign was carried out with the upgraded ODI camera on WIYN, which was commissioned in 2015 and which provides a field of view (FOV) more than three times larger than that of pODI. In a series of observing runs between 2015 and 2021, we acquired deep WIYN ODI images of more than 30 additional UCHVC targets in two broadband filters (SDSS g and i). During this phase of the project, we made improvements to our detection and analysis methods and then applied the updated methods to the ODI sample of objects. We also used the improved methods to reanalyze the imaging data of the five UCHVCs in the pODI sample for which J19 identified potential stellar counterparts.

In this paper, we present the results from the second and final phase of our campaign to obtain follow-up optical imaging of ALFALFA UCHVCs. In Section 2, we describe the selection criteria and properties of the UCHVCs we observed and analyzed. Section 3 summarizes the procedures we used to acquire imaging observations and produce source catalogs and calibrated broadband optical photometry for each UCHVC field. In Section 4, we describe the steps we carried out to search for stellar counterparts to the H I sources and to assess the significance and validity of the dwarf galaxy candidates that we have identified. We also discuss the improvements that were made to our analysis methods in the second phase of the project. Section 5 presents the full results of this analysis. In the last section of the paper, we examine our results in the context of recent relevant theoretical work and other observational studies aimed at detecting and studying gas-rich dwarf galaxies in and around the Local Group.

2. The Sample of UCHVCs Analyzed for This Work

The UCHVCs we observed were drawn from the ALFALFA survey data (Haynes et al. 2018) using criteria laid out in detail in Adams et al. (2013). The primary criteria that were used to select sources are as follows:

1. The source must have an H I major axis, a, less than 30′ in order to have a size consistent with expectations for the baryonic component of low-mass dark matter halos. This corresponds to a diameter of ∼2 kpc at a distance of 250 kpc, ∼9 kpc at 1 Mpc, and ∼20 kpc at 2.5 Mpc.
2. The source must have an ALFALFA signal-to-noise ratio greater than 8, as defined in Equation 2 in the ALFALFA 40% catalog (Haynes et al. 2011).
3. The source must have no more than three neighboring H I structures within 3° on the sky or 15 km s^{-1} in velocity space in order to ensure that it is sufficiently isolated. It must also have at least a 15° separation from any previously known HVC complexes.
4. The source must have a heliocentric velocity between −500 and 1000 km s^{-1}, so that it is likely to reside in the Local Volume.
5. The source must have an absolute velocity with respect to the local standard of rest (LSR) greater than 120 km s^{-1}, to avoid contamination with Galactic HVCs. This criterion was in some cases relaxed when all other criteria were met, since some nearby dwarf galaxies have velocities lower than this value (e.g.,Leo T,with $v_{\rm LSR}$ ∼60 km s^{-1}; Irwin et al. 2007; Ryan-Weber et al. 2008).
6. The source must have no clear optical counterparts in either SDSS or DSS.

Approximately 100 ALFALFA sources were identified as UCHVCs, and we selected a sample of roughly 60 sources from that original list that were best suited for optical follow-up (e.g., strong H I detections, relatively high column densities, and/or potentially interesting for other reasons, such as sky position or velocity); see J19 for more details about how the optical follow-up sample was selected. As mentioned in Section 1, 23 of these objects were analyzed in the first phase of the project and presented in J19. We observed 35 more objects after the pODI instrument was replaced with ODI. The substantially larger FOV of ODI (see Section 3) necessitated modifications to our processing and detection steps, so it made sense to split the project into two phases in this way.

The final sample of objects being presented here includes 25 objects that were observed with ODI and for which we were

Table 1
Sample of UCHVCs Analyzed for This Work

Name	R.A.	Decl.	S_{21} (Jy km s^{-1})	cz (km s^{-1})	w_{50} (km s^{-1})	$\bar{a}$ ($'$)	log $\bar{N}_{\rm HI}$ (atoms cm^{-2})	log$M_{\rm HI}$ ($M_\odot$)	Obs. Date	Detection
AGC102994	$00^h54^m31\overset{s}{.}6$	$+29^d24^m02^s$	0.58 ± 0.03	-290	23 ± 2	5.70	18.90	5.14	2016B, 2017B	ND
AGC115710	$01^h26^m21\overset{s}{.}5$	$+05^d23^m08^s$	4.81 ± 0.04	59	21 ± 1	8.65	19.45	6.05	2016B	PD
AGC116548	$01^h06^m00\overset{s}{.}7$	$+12^d26^m57^s$	0.96 ± 0.03	84	11 ± 1	6.15	19.05	5.35	2015B	ND
AGC122834	$02^h03^m48\overset{s}{.}8$	$+29^d13^m13^s$	3.58 ± 0.06	49	16 ± 5	10.70	19.14	5.93	2016B	ND
AGC122835	$02^h05^m35\overset{s}{.}5$	$+29^d13^m56^s$	1.23 ± 0.04	29	23 ± 5	5.60	19.24	5.46	2016B	PD
AGC174764	$07^h56^m14\overset{s}{.}8$	$+25^d09^m00^s$	0.64 ± 0.04	174	21 ± 1	7.00	18.76	5.18	2016B	ND
AGC198683	$09^h32^m08\overset{s}{.}0$	$+23^d37^m52^s$	0.88 ± 0.04	178	19 ± 1	11.10	18.50	5.32	2016B	ND
AGC208315	$10^h27^m01\overset{s}{.}1$	$+08^d47^m08^s$	4.96 ± 0.07	148	20 ± 2	12.60	19.14	6.07	2017A	PD
AGC208524	$10^h47^m02\overset{s}{.}5$	$+01^d46^m31^s$	0.67 ± 0.03	179	14 ± 1	4.85	19.10	5.20	2016A, 2017A	ND
AGC208752	$10^h23^m09\overset{s}{.}0$	$+20^d40^m59^s$	1.79 ± 0.03	-60	16 ± 1	7.60	19.13	5.63	2019A	ND
AGC219214	$11^h09^m29\overset{s}{.}8$	$+05^d26^m01^s$	0.56 ± 0.03	142	20 ± 5	5.55	18.90	5.12	2019A	ND
AGC227977	$12^h09^m20\overset{s}{.}0$	$+04^d23^m30^s$	0.57 ± 0.05	-143	18 ± 4	10.00	18.40	5.13	2014A	ND
AGC227988	$12^h46^m22\overset{s}{.}9$	$+04^d48^m42^s$	0.49 ± 0.05	320	48 ± 10	4.70	18.99	5.06	2019A	ND
AGC233763	$13^h12^m42\overset{s}{.}3$	$+13^d30^m46^s$	0.78 ± 0.04	129	31 ± 6	5.30	19.09	5.26	2017A	ND
AGC233831	$13^h22^m41\overset{s}{.}6$	$+11^d52^m31^s$	0.63 ± 0.02	124	16 ± 1	4.50	19.14	5.17	2018A	ND
AGC249283	$14^h23^m57\overset{s}{.}7$	$+05^d23^m40^s$	1.11 ± 0.07	252	32 ± 9	13.50	18.43	5.42	2019A	PD
AGC257994	$15^h53^m54\overset{s}{.}0$	$+14^d41^m48^s$	2.04 ± 0.04	146	23 ± 3	9.65	18.98	5.68	2021A	ND
AGC268067	$16^h05^m29\overset{s}{.}4$	$+16^d09^m12^s$	1.94 ± 0.05	158	35 ± 7	8.40	19.08	5.66	2018A	ND
AGC268071	$16^h12^m36\overset{s}{.}8$	$+14^d12^m26^s$	2.67 ± 0.08	109	62 ± 15	9.75	19.09	5.80	2018A	BD
AGC268213	$16^h22^m35\overset{s}{.}7$	$+05^d08^m48^s$	2.90 ± 0.06	-139	18 ± 4	10.85	19.03	5.83	2017A	ND
AGC333604	$23^h11^m23\overset{s}{.}2$	$+27^d56^m45^s$	1.74 ± 0.03	66	19 ± 2	7.65	19.12	5.61	2018B	ND
AGC333651	$23^h55^m21\overset{s}{.}4$	$+25^d17^m26^s$	0.87 ± 0.03	45	14 ± 4	7.85	18.79	5.31	2015B	ND
AGC334257	$23^h02^m11\overset{s}{.}3$	$+16^d00^m48^s$	0.68 ± 0.04	-452	22 ± 11	7.95	18.68	5.20	2018B	ND
AGC335755	$23^h14^m16\overset{s}{.}4$	$+03^d23^m07^s$	7.95 ± 0.10	42	23 ± 1	13.15	19.31	6.27	2018B	ND
AGC501816	$10^h05^m19\overset{s}{.}4$	$-00^d02^m26^s$	1.70 ± 0.05	107	20 ± 1	7.15	19.17	5.60	2019A	ND
AGC749140	$00^h51^m16\overset{s}{.}4$	$+15^d11^m11^s$	1.33 ± 0.03	52	17 ± 4	5.95	19.22	5.50	2018B	PD

Note. Following Haynes et al. (2018), the adopted error on the recessional velocities listed in column 5 is half of the w_{50} error. The H I mass values in column 9 are calculated at an assumed distance of 1 Mpc. In the "Detection Status" column, objects for which no detection in the field meets our lower-threshold criteria are listed as ND; this includes the UCHVC AGC 501816, which is located near the globular cluster Pal 3, and which is discussed in Section 5.1.2. Objects categorized as having a possible detection are listed as PD, and objects with our best (most convincing) detections are listed as BD; see Section 4.3 for more information about the categories.

able to obtain a complete set of observations, i.e., high-quality, deep imaging in both filters (g and i). In addition, we include one more UCHVC (AGC 227977) that already had existing pODI imaging data, but that we had planned to re-observe with ODI under better sky conditions. We were not able to acquire a complete set of high-quality ODI images for this object, but in the end we deemed the existing pODI images to be of sufficient quality that we could include the object in the current sample. Nine more UCHVCs were observed, but the imaging data could not be fully analyzed for a range of reasons (e.g., observed under poor sky conditions, good-quality images obtained in only one filter); the objects are mentioned here for completeness.

The ALFALFA-derived properties of the 26 UCHVCs we analyzed for the second phase of the project are presented in Table 1. The table includes the source designation, sky position, H I line flux ($S21$), recessional velocity (cz), H I line FWHM (W_{50}), mean angular diameter of the H I detection (a), mean H I column density ($\log N_{\rm HI}$), H I mass at an assumed distance of 1 Mpc, the dates of the observations, and the detection status from our analysis.

Information about the nine other UCHVCs that could not be analyzed as part of this phase of the project are presented in Table 2. The columns are the same as those shown in Table 1 except that no detection status is given since a full analysis could not be done. We include information about the observations we were able to acquire when applicable. The objects that fall into this category typically had poor-quality data and/or imaging in only one filter.

Table 1 shows that the objects we analyzed possess a fairly broad range of H I properties. The objects in our sample have H I flux values that range from 0.49−7.95 Jy km s^{-1}, with most sources between 0.6 and 2.0 Jy km s^{-1}. In general, we prioritized H I sources with higher column densities during the data acquisition phase of the project, under the assumption that these targets would be more likely to host a dwarf galaxy; one (albeit indirect) consequence of this is that the sources we were unable to analyze because of insufficient data (Table 2) tend to have smaller total H I fluxes than the objects in the sample shown in Table 1. The H I major axes of our objects range from $5\farcm3-17\farcm2$ (approximately 1.5–5.0 kpc at a distance of 1 Mpc), and they span a recessional velocity range from -452 to $+320$ km s^{-1}.

3. Observations and Initial Data Reduction

We obtained optical imaging of the UCHVC sources with the WIYN 3.5 m telescope at Kitt Peak National Observatory over the course of several observing seasons; the year and semester of the observations of each source are given in Table 1. Observations carried out prior to 2015 were taken with pODI, which had a central imaging area that consisted of a 3–3 array of orthogonal transfer arrays (OTAs). Each individual OTA comprises an 8–8 grid of CCD detectors. The pODI configuration provided a $24'$ by $24'$ FOV and a pixel scale of

Table 2
UCHVCs With Insufficient Data to Include in the Sample

Name	R.A.	Decl.	S_{21} (Jy km s^{-1})	cz (km s^{-1})	w_{50} (kms^{-1})	$\bar{a}$ ($'$)	log $\bar{N}_{HI}$ (atoms cm^{-2})	logM_{HI} ($M_\odot$)	Obs. Date
AGC219663	$11^h34^m29\overset{s}{.}7$	$+20^d12^m49^s$	0.75 ± 0.03	74	17 ± 1	7.35	18.79	5.25	2013A
AGC229327	$12^h32^m31\overset{s}{.}6$	$+17^d57^m21^s$	1.02 ± 0.05	251	25 ± 1	12.95	18.43	5.38	2013A
AGC232765	$13^h23^m09\overset{s}{.}4$	$+15^d11^m17^s$	1.37 ± 0.03	105	23 ± 3	5.15	19.36	5.51	2016A
AGC249326	$14^h31^m58\overset{s}{.}8$	$+06^d35^m20^s$	0.70 ± 0.04	136	38 ± 11	5.65	18.98	5.22	N/A
AGC249393	$14^h10^m58\overset{s}{.}1$	$+24^d12^m04^s$	1.01 ± 0.06	−156	36 ± 1	11.90	18.50	5.38	2013A
AGC249441	$14^h07^m00\overset{s}{.}8$	$+00^d13^m23^s$	0.74 ± 0.04	−131	16 ± 2	8.40	18.66	5.24	*g*: 2019A
AGC249565	$14^h35^m57\overset{s}{.}6$	$+17^d10^m04^s$	1.76 ± 0.04	30	18 ± 1	7.65	19.12	5.62	2013A
AGC257956	$15^h55^m07\overset{s}{.}5$	$+14^d29^m29^s$	1.54 ± 0.04	144	25 ± 6	6.70	19.18	5.56	*i*: 2017A
AGC258241	$15^h08^m24\overset{s}{.}4$	$+11^d24^m22^s$	0.98 ± 0.07	163	19 ± 2	12.70	18.43	5.36	N/A

Note. The adopted error on recessional velocities listed in column 5 is half of the w_{50} error according to Haynes et al. (2018). The H I mass values in column 9 are calculated at an assumed distance of 1 Mpc.

$0\overset{''}{.}11$ pixel^{-1}. The upgraded ODI camera includes a 5–6 arrangement of OTAs, yielding a 40′–48′ FOV and the same pixel scale as pODI.

Each of the UCHVCs was imaged with a series of nine 300 s exposures in both the SDSS *g* and *i* filters, and the telescope was dithered slightly between exposures in order to fill in the gaps between the CCD detectors and the OTAs; this yielded a total integration time of 45 minutes in each filter. The images were transferred to the One Degree Imager Pipeline, Portal, and Archive (ODI-PPA) system[9] (Gopu et al. 2014; Young et al. 2014) for storage and processing. The QuickReduce data reduction pipeline (Kotulla 2014) was used to carry out pixel masking, crosstalk and persistence correction, overscan subtraction, bias and dark subtraction, flat-field correction, pupil ghost correction, and cosmic-ray removal on the images.

After the QuickReduce processing, the images were further reduced and stacked using the odi-tools software routines, a suite of Python routines developed by William Janesh and Owen Boberg to help facilitate the analysis of the J19 UCHVCs sample and other pODI and ODI data (Janesh 2018). The images were illumination-corrected and reprojected to the same pixel scale and coordinate reference frame. Sets of images taken in the same filter were then scaled to a common flux level and combined into a single science-ready image. The combined images in the two filters were aligned and then trimmed to 20,000 pixels by 22,000 pixels (∼37′–40′) to cut out the regions without full coverage in the dither pattern. The mean FWHM of the point-spread function (PSF) in the final combined images was typically $\lesssim 1\overset{''}{.}0$ in both filters. In cases where we observed an object on multiple nights with varying sky conditions, we used the images with the best seeing values to construct the final combined image in a given filter.

All of the UCHVC targets fall within the footprint of SDSS, so we measured the magnitudes and colors of several hundred SDSS stars that appeared within each of the ODI frames in order to derive photometric calibration coefficients (zero-points and color terms) that we could then use to calculate calibrated magnitudes and colors for the other sources in the final combined images. Typical uncertainties on the photometric zero-points in the calibrated *g* and *i* magnitude equations are ∼0.02 mag.

[9] The ODI Portal, Pipeline, and Archive (ODI-PPA) system is a joint development project of the WIYN Consortium, Inc., in partnership with Indiana University's Pervasive Technology Institute (PTI) and NSFs NOIRLab.

4. Searching for Stellar Populations Associated with the H I Clouds

4.1. Applying a Color–Magnitude Diagram Filter to the Stellar Catalogs

When we analyze our optical images of the UCHVCs, the goal is to search for collections of stars—which we refer to as "stellar overdensities" —with properties like those of the stellar populations one would expect to be associated with a Local Group dwarf galaxy. We have developed a largely automated procedure to carry out this search as well as to characterize the statistical significance of any stellar overdensities we find. The overall method we use was laid out in Janesh et al. (2015); as mentioned earlier, we have since made some improvements to the method, which are described in this section. Additional details can be found in Smith (2022).

We use a processing pipeline that calls Python routines and IRAF tasks and includes both automated steps and steps that require input from the user. The main steps in the process are as follows. First, we carry out detection and aperture photometry of the sources in the WIYN images that are above a certain count threshold—typically, 3.5–4 times the standard deviation of the sky background level in the images. The source lists generated from the two images are then matched, and extended objects are eliminated based on the difference in magnitudes measured in two different apertures. We measure the instrumental magnitude of each source using a small aperture with a radius equal to the average FWHM of the image (magnitude *m*1) and a larger aperture with a radius equal to twice that value (magnitude *m*2). Bright point sources fall along a clearly defined sequence when plotted in the *m*2 versus *m*1–*m*2 plane; we use that sequence to define the center of our selection region and then select sources within 2.5σ of that center. The selection region is thus wider at fainter magnitudes where the photometric uncertainties are larger; see Janesh (2018) and Smith (2022) for more details. Aperture photometry of the point sources that survive the extended source cut is then carried out in both images, using an aperture radius equal to the average FWHM PSF of the image. An aperture correction is computed from photometric measurements of selected bright stars across the image and then applied to the instrumental magnitudes of all of the point sources. Final calibrated

magnitudes and colors are calculated for each point source in the field by applying the appropriate photometric calibration coefficients along with Galactic extinction corrections calculated from the Schlegel et al. (1998) dust maps and the relations in Schlafly & Finkbeiner (2011). Typical 5σ detection limits in the images are $g \sim 25.4$ mag and $i \sim 24.4$ mag.

Next we construct a CMD filter that can be applied to the final photometry catalog for a given field. The construction of the filter was described in detail in Janesh et al. (2015) and followed the basic method outlined in Walsh et al. (2009) using stellar isochrones from Girardi et al. (2004). Because UCHVCs are expected to host old, metal-poor stars, the CMD filter is designed to select stars with ages between 8 and 14 Gyr and metallicities between $Z = 0.0001$ and 0.0004. In Janesh et al. (2015), we used our WIYN observations of Leo P to test the CMD filtering method and demonstrated that the filter and our detection methods are effective at finding a stellar population that consists of only a modest population of red giant branch (RGB) stars. The position and extent of the filter on the CMD is defined by the locations of the isochrones for the chosen age and metallicity ranges, as well as by the distance to the putative stellar population. We shift the filter in the vertical (magnitude) direction on the CMD over a range of magnitudes in increments of 0.01 mag, to cover a corresponding distance range of 250 kpc to 2.5 Mpc. Applying the CMD filter at each distance step to our photometric catalog yields a subset of stars in a given UCHVC field that, given their g and i photometric measurements and associated uncertainties, lie in a region of the CMD that is consistent with the location and boundaries of the filter. Figure 1 shows an example of a CMD filter being applied to our data; the black dots show the CMD positions of the point sources that appear in one of the UCHVC fields, the blue solid line marks the location of the CMD filter corresponding to a distance of 400 kpc and the age and metallicity ranges mentioned above, and the red dots are the sources that are selected by the CMD filter in this case.

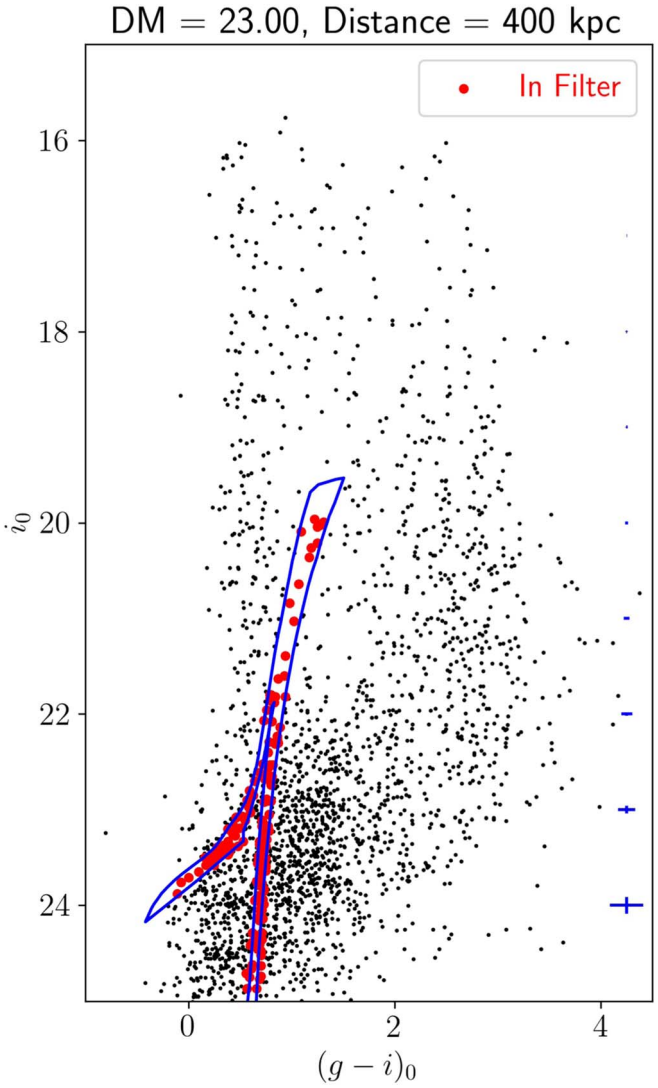

Figure 1. An example of the CMD filter that is applied to the photometric catalog derived from the WIYN ODI imaging of each UCHVC field in order to select stars with properties expected for a dwarf galaxy at a given distance (see Section 4.1). Black points are point sources located within the images, and red points are those that coincide with the location of the filter given their g and i magnitudes and associated 1σ uncertainties. Error bars showing the typical photometric uncertainties at various magnitudes are plotted in blue on the right-hand side. The filter shown in this example corresponds to a distance of 400 kpc.

4.2. Searching for Overdensities in the Spatial Distribution of CMD-filtered Stars

Once we have identified the set of stars selected by a given CMD filter, we search for clustering among the stars to identify any stellar populations that might be associated with the H I source. We begin by smoothing the spatial distribution of the stars with a Gaussian kernel. We use smoothing kernels with a diameter of both $2'$ and $3'$ in order to mimic the range of typical angular sizes that a dwarf galaxy might have if it were located within the distance range being probed. We then estimate the density of stars at each location in the smoothed image as a function of the mean density of the CMD-filtered stars across the image. Any region of the image where the stellar density exceeds the mean value represents a potential stellar overdensity associated with the H I source.

In order to determine the significance of a given overdensity (i.e., how likely it is to be a genuine overdensity rather than a result of random fluctuations in the point-source spatial distribution), we carry out a series of 10,000 Monte Carlo experiments corresponding to each CMD filter position. We distribute the same number of CMD-filtered stars at random locations across the field and repeat the smoothing steps. Any overdensity identified in the real data can then be compared to those found in the randomly generated data. The significance of the overdensity in the real data is quantified by calculating the number of overdensities in the random realizations that are less dense than the real overdensity. After carrying out these steps for every distance and for both smoothing radius sizes, we can compare the overall results across the entire parameter space that has been searched and look for the most significant detections that appear within a given UCHVC field.

4.3. Assessing the Detected Stellar Overdensities and Cross-Matching with the Gaia and SDSS Catalogs

The next stage of the analysis includes a variety of steps that are applied as appropriate, depending on the results of the CMD filtering and smoothing process. The first step in all cases is to examine the location and significance of the overdensities revealed by the CMD filtering process at every step of the distance range being sampled (250 kpc to 2.5 Mpc). We focus on detections that have high significance (approximately 90%

or higher) and that are close in projection to the H I centroid position—usually within 8′, which translates to a separation of 2.3 kpc at a distance of 1 Mpc. We sometimes consider overdensities that have significance in the 80%–90% range, or are up to 10′ away from the H I centroid, if their other characteristics suggest they could be a genuine dwarf galaxy candidate. If no overdensities are found that meet these criteria, we classify the UCHVC target as a nondetection and do not carry out any further analysis on the imaging data for that UCHVC. If multiple unique detections (i.e., at different sky positions and/or distances) are found, each is assessed with the next steps. We note also that the steps described here are carried out on the results produced using both of the smoothing kernels (i.e., smoothing kernels with diameters of 2′ and 3′), and we take the results derived from both kernel sizes into account when selecting and classifying the various overdensities that are identified.

Once we have identified possible stellar overdensities associated with the H I sources, we examine the properties of the individual stars that are within 3′ of the center of the detected overdensity. We look at the CMD locations of the stars that compose the detection to judge whether the stars match the expected morphology of the RGB of a genuine dwarf galaxy at the specific distance to which the filter location corresponds. We generally look for a detected overdensity that has stars that populate a fair fraction of the RGB region of the CMD filter, as well as stars that lie in the horizontal branch (HB) region when applicable. We also compare the numbers and positions of the stars in the detected overdensity to those of the stars in a reference circle of similar size that is placed at a random location near the edges of the image, far from the H I centroid position (to ensure that it does not overlap with any detection circles). If the CMD of the stars in the detection circle is similar in appearance and number of stars to the CMD of the reference circle, then the detection is deemed less convincing.

We also inspect how closely the stars within the detection CMD are clustered on the image. In some cases, the stars that comprise a given detected overdensity may not actually be very close to each other spatially (e.g., the detection might consist of several stars that are scattered around the edges of a particular smoothed region that makes up the detected overdensity), which makes the detection less convincing as a genuine dwarf galaxy candidate. In addition, we examine the radial profiles of the individual stars within the detection, and the objects in the region around the detection area, because in some cases (for example), clusters of faint, distant unresolved background galaxies can masquerade as collections of nearby stars with colors like RGB stars. To help with this step, we also perform a quick cross-reference of the stars within the overdensity with source catalogs from the SDSS survey, to see whether the sources in and around the detection are actually galaxies. Finding a detected overdensity that is close (in projection) to an obvious background galaxy group or cluster suggests that the detection may actually be made up of unresolved background galaxies rather than being a genuine stellar association in or near the Local Group.

After these steps are completed, the UCHVC targets with detected overdensities are assigned into separate categories based on our initial assessment of the likelihood that we may have detected the presence of a genuine dwarf galaxy. UCHVCs with overdensities that no longer seem convincing after these checks are designated as "nondetections" (see Table 1) and are not analyzed further.

For the UCHVC targets that remain, we cross-match the point-source catalogs with the Gaia[10] EDR3 catalog (Gaia Collaboration et al. 2016, 2021) and remove foreground stars (by rejecting any source with a proper motion greater than three times the uncertainty on that quantity) as well as known active galactic nuclei (AGNs; by removing sources that match those in the list of AGNs used to calibrate the Gaia EDR3 celestial reference frame; Gaia Collaboration et al. 2021). We also make use of the star/galaxy classification in the SDSS catalog to remove any sources that are likely to be galaxies. Before implementing the latter step, we examined how reliable the SDSS star/galaxy classification was by comparing it to the classification used by the Cosmic Assembly Near-infrared Deep Extragalactic Legacy Survey[11] (CANDELS; Grogin et al. 2011; Koekemoer et al. 2011; Stefanon et al. 2017). CANDELS was carried out with the Hubble Space Telescope (HST), and therefore genuine point sources can be distinguished from background galaxies more effectively in CANDELS data than in data from a ground-based survey. We found that for sources in common between SDSS and CANDELS, the CANDELS star/galaxy classification matched the SDSS classification >94% of the time. Since misidentification occurred for only a small fraction of sources, and the number of objects in our source lists that are identified as galaxies in SDSS is also relatively small, we decided that applying the SDSS classification to our source lists was warranted because it would help us weed out spurious dwarf galaxy candidate detections. Figure 2 shows that the majority of sources that are eliminated when we cross-match our point-source catalogs with Gaia EDR3 and SDSS are bright (with $i <$ about 20 mag) and are excluded because they are Galactic foreground stars.

After removing the contaminants found in the catalog cross-matching, we repeat the CMD filtering and smoothing steps, again assess each overdensity that is detected in a given UCHVC field, and update the initial classification that was assigned. The final results of the search process are sorted into three categories: "nondetections" (UCHVCs that have no convincing evidence for an optical counterpart); "possible detections" (UCHVCs that may have an optical counterpart that warrants further follow-up), and "best detections" (UCHVCs that have a convincing or likely optical counterpart).

For objects that fall within the latter two categories, we estimate the H I and optical properties for the UCHVC and its counterpart at the relevant distance. We take the distance of the object to be the CMD filter distance that corresponds to the most significant detection that occurs for a given overdensity. We also tabulate the range of distances over which a given detection remains above some threshold for significance—90% for overdensities that have a peak significance $\geqslant$ 90%, and 80% for overdensities with a peak significance between 80–90%—

[10] This work has made use of data from the European Space Agency (ESA) mission Gaia (https://www.cosmos.esa.int/gaia), processed by the Gaia Data Processing and Analysis Consortium (DPAC, https://www.cosmos.esa.int/web/gaia/dpac/consortium). Funding for the DPAC has been provided by national institutions, in particular the institutions participating in the Gaia Multilateral Agreement.

[11] This work is based on observations taken by the CANDELS Multi-Cycle Treasury Program with the NASA/ESA HST, which is operated by the Association of Universities for Research in Astronomy, Inc., under NASA contract NAS5-26555.

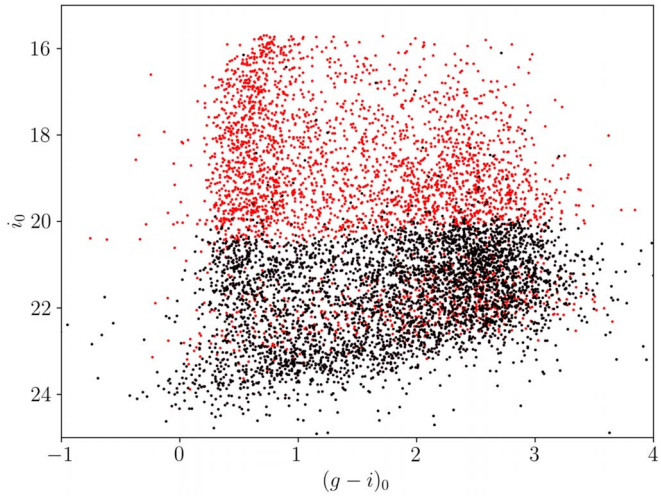

Figure 2. An example of the effect of the cross-matching step that is carried out on source catalogs of fields in which potential stellar overdensities have been identified. Sources in the field are cross-matched with Gaia and SDSS catalogs in order to identify and remove contaminating foreground objects (Galactic stars) and background objects (galaxies and AGNs) from our star lists. Sources that are retained are shown with black points, and sources that are removed are shown with red points. In this example field, approximately one-third of the objects in our original source list were removed as likely Galactic stars and ∼10% were removed as likely background galaxies or AGNs; these percentages are fairly typical, although the exact proportions of foreground and background objects and remaining point sources depend on quantities like the Galactic latitude and exact detection limits of each set of images.

and use this to help define an uncertainty on the estimated distance (see Sections 5 and 6).

4.4. Quantifying the Detection Completeness

As part of the analysis, we carry out artificial star tests to quantify the photometric depth and detection limits of each set of UCHVC images. Before running the full set of tests, we confirmed that completeness testing performed on a 4000×4000 pixel subsection of the images yields the same results as tests performed on the full-size ODI images. Since source crowding is not an issue in our UCHVC target fields (they are empty of strongly clustered sources, with the exception of a field that includes the globular cluster Pal 3; see Section 5.1.2 for more discussion), we found that running artificial star tests on portions of the images is a valid approach. The rest of the steps were carried out on these smaller-sized images.

We characterized the PSF within each of the images by fitting the light distributions of several dozen bright but unsaturated stars within the frames. We then generated artificial stars and injected them into the images, 400 stars at a time in steps of 0.2 mag, until we had spanned the range of stellar magnitudes present in the real data. We followed our detection procedures to recover and measure the magnitudes of the artificial stars and used that information to create a completeness curve (which quantifies the proportion of stars recovered as a function of magnitude) for that image and filter. We created 50% completeness curves for the CMD of a given UCHVC field by combining the completeness information in each of the filters. Specifically, we constructed a grid of i and g–i values and then computed the completeness at a given position in the grid by multiplying the i-magnitude completeness by the appropriate completeness in the g filter based on the color at that grid position; for example, for the point at $i = 25$ mag and g–$i = 1$, we multiplied the detection completeness in i at 25 mag by the completeness in g at 26 mag. We carried out this calculation over the entire range of source magnitudes and colors that appear in our CMDs (i.e., $i \geqslant 26$ mag, g–i from -1.5 to $+4$). We then interpolated between the grid values to define the 50% completeness curve for a given UCHVC field. These 50% completeness curves are included in the results presented in Section 5.

4.5. Changes to the Original Detection Methods

Before analyzing the WIYN ODI data set, we examined each of the detection steps carried out on the J19 sample to explore whether modifying the steps might increase our chances of detecting dwarf galaxy candidates associated with the UCHVCs. We made two substantial modifications to our process.

The first was a change in the CMD filtering step. As described in Section 4.1, the boundaries of the CMD filter are defined by the set of isochrones that characterizes the expected stellar population of a UCHVC. When we apply the filter, we select sources that have i magnitudes and g–i colors that would fall within the filter given the relevant photometric uncertainties. When we examined this step in the detection process, we discovered a numerical error in the original code that was applied to the J19 WIYN pODI data, which made the CMD filter less restrictive than intended. The effect of the error was more pronounced at faint magnitudes, where the photometric errors are large, but the impact was mitigated because the code also included a photometric error cut that removed sources with i-magnitude errors $\geqslant$0.2 mag or g–i color errors $\geqslant$0.28 mag. Nevertheless, the end result of this coding error was that the pODI data set yielded a relatively large number of detections that were later rejected as false when they were examined individually.

After correcting this error and then testing various options for how to apply the CMD filter to the ODI imaging data, we decided to implement a relatively restrictive source selection, allowing only those objects that are consistent with the boundaries of the CMD filter given the 1σ photometric errors of the object. We also implemented a change so that the code uses the uncertainties in the g magnitude and i magnitude (instead of the uncertainties in the i magnitude and g–i color, as was the case in the original code) to determine whether a source should be accepted. More specifically, we imposed the condition that sources were selected only if the g-magnitude and i-magnitude errors were both $\leqslant$ 0.2 mag. This prevented sources with, for example, small i uncertainties but larger g uncertainties from passing the filtering step. The final result is a more restrictive CMD filter than the filter originally applied to the J19 pODI data set; the revised filtering process only selects stars with reliable photometry in both filters that match closely with the metallicity and age range of the expected stellar population, which reduces the number of spurious detections appearing in each of the UCHVC fields.

The second major change made to the detection process was to add the cross-matching between our sources and objects in the Gaia and SDSS catalogs that was described in Section 4.3. This added step serves to much more effectively remove both foreground and background contaminants from each of the UCHVC fields (see Figure 2), which was especially helpful for processing the ODI data set, given the large FOV and the large numbers of sources detected in each field.

We used the improved series of steps to process all of the objects in the ODI sample listed in Table 1. We also decided to reanalyze the WIYN pODI imaging data for the five UCHVCs in the J19 sample that yielded possible dwarf galaxy candidates. Results from the current sample of UCHVCs, as well as the r-analysis of the five pODI objects from J19, are presented in the next section.

5. Results

5.1. Results for the Sample of UCHVCs Analyzed for This Work

We carried out the above-described processing and analysis steps for the 26 objects in the sample listed in Table 1. Twenty of the UCHVCs in this sample had no stellar overdensity in the images that satisfied our criteria for a dwarf galaxy candidate, and are thus classified as "nondetections" and labeled "ND" in the table. The first 19 nondetections are discussed in Section 5.1.1, and one object in this category warrants a separate discussion in Section 5.1.2. Five objects classified as "possible detections" are described in Section 5.1.3, and the one object classified as a "best detection" is discussed in Section 5.1.4.

5.1.1. Objects Classified as "Nondetections"

For most of the objects in this category, the classification was straightforward because no stellar overdensities were found that had significance in the ∼80%−90% range or higher and were near the H I centroid. In a few other cases, significant overdensities were identified initially, but then not found to be believable upon close inspection of the individual sources located within the overdensity and in the surrounding region. One object (AGC 335755) made it through the first round of screening to the final stages of analysis—i.e., the cross-matching with the Gaia and SDSS catalogs—but was no longer deemed convincing after the contaminating foreground and background objects were removed from the source list. In any case, these 19 UCHVCs show no evidence that they host a dwarf galaxy candidate within the distance range that we tested (250 kpc to 2.5 Mpc), given the detection limits of our images. We note that other searches for optical counterparts to compact H I clouds have detected dwarf galaxies at larger distances (∼3 −20 Mpc; Bellazzini et al. 2015a, 2015b; Sand et al. 2015; Tollerud et al. 2015), so there is still the possibility that these UCHVCs are associated with a stellar counterpart that is farther away than 2.5 Mpc and therefore beyond the scope of our survey. On the other hand, our images of the UCHVCs in this category contain no faint optical counterparts (either resolved-star counterparts or unresolved faint optical emission) like the ones detected in those studies.

5.1.2. An H I Cloud Near in a Globular Cluster?

One more UCHVC in the "nondetection" category requires a more detailed discussion. AGC 501816 was included in the ODI sample because it lacked an obvious optical counterpart, and its other properties satisfy the criteria for UCHVCs, except that its $|v_{\rm LSR}|$ value, 99 km s^{-1}, is below the nominal 120 km s^{-1} minimum requirement. In addition to being of interest as a possible compact H I cloud, AGC 501816 is notable because of its proximity to the Milky Way globular cluster (GC) Pal 3. The centroid of the H I source lies 7.3′ away in projection from Pal 3 and the GC appears within our ODI images. This projected angular separation translates to only 195 pc at the distance of Pal 3 (91.9 kpc; Hilker 2006). Moreover, the GC and the UCHVC have similar heliocentric velocities: Pal 3 has a $v_{\rm helio}$ of 94.0 ± 0.8 km s^{-1}, only 13 km s^{-1} below that of AGC 501816 (Table 1).

Pal 3 is located in the outer stellar halo of the Milky Way and is one of only five Galactic GCs with galactocentric distances of ∼90 kpc or greater (Harris 1996, 2010 edition). It is fairly faint for a GC, with $M_V = -5.7$ (Harris 1996, 2010 edition), has a modest mass (1.9–10^4 $M_\odot$; Baumgardt & Hilker 2018), and is markedly extended in size, with a half-light radius (r_h) of ∼0.′7 (Baumgardt & Hilker 2018), or ∼19 pc at the 91.9 kpc distance. This is several times larger than the median half-light radii of the GCs in both the Milky Way and Andromeda, which is ∼2−3 pc (van den Bergh 2010). CMD fitting indicates that the cluster belongs to the metal-poor subpopulation of the Milky Way GC system, with [Fe/H] = −1.7, and has an estimated age of ∼10 Gyr (Hilker 2006). The location and orbital properties of Pal 3 have prompted studies of its origin, with some concluding that it may have been accreted into the outer Galactic halo along with its parent dwarf satellite galaxy (Palma et al. 2002), and others suggesting it could have been ejected from the Phoenix dwarf irregular galaxy and captured by the Milky Way (Sharina et al. 2018). However, stellar abundance studies seem to suggest instead that Pal 3 coevolved with the rest of the Galactic GC system (Koch et al. 2009).

It has long been understood that GCs like Pal 3 and the other members of the Galactic GC system may contain gas and dust that originated in the outer atmospheres of evolved stars and was subsequently lost to the interstellar medium within the cluster (e.g., Roberts 1959, 1960). Much of the gas is expected to be removed from the GCs through a variety of mechanisms, including winds from stars and stellar remnants, and dynamical pressure as the cluster orbits the Galaxy (e.g., Frank & Gisler 1976; Spergel 1991). However some gas may remain and be detectable as, for example, diffuse atomic hydrogen that emits 21 cm radiation, or perhaps hotter gas that produces UV or X-ray emission.

Many searches have been carried out over the past several decades using a range of approaches to look for hydrogen gas in and around Milky Way GCs; in general, these studies have had limited success, often resulting in upper limits or ambiguous detections (e.g., Heiles & Henry 1966; Kerr & Knapp 1972; Knapp et al. 1973; Erkes & Philip 1975; Birkinshaw et al. 1983; Faulkner et al. 1991; Freire et al. 2001; van Loon et al. 2006, and many others). One study of particular relevance is van Loon et al. (2009), which was carried out as part of the Galactic Arecibo *L*-band Feed Array (GALFA) survey. van Loon et al. (2009) observed four GCs and set 3σ limits of 6−51 $M_\odot$ on the amount of gas in the four clusters, and also identified a compact high-velocity H I cloud roughly 1° away from the outer halo GC Pal 4. They conclude that the cloud may be physically associated with Pal 4 or may simply be a chance superposition, since the two objects differ by ∼40 km s^{-1} in velocity and the cloud has a relatively large separation (∼2 kpc) and a high H I mass (3–10^6 $M_\odot$) if it is actually at the same distance as Pal 4 (109 kpc).

In Figure 3, we show the location of Pal 3 and the UCHVC AGC 501816 in our ODI images. The ALFALFA H I ellipse is marked, as are the tidal and half-light radii of the globular cluster. We analyzed the ODI imaging data of this field in two ways: with the stars that make up Pal 3 included in the source lists, and with the stars in Pal 3 removed. The first approach

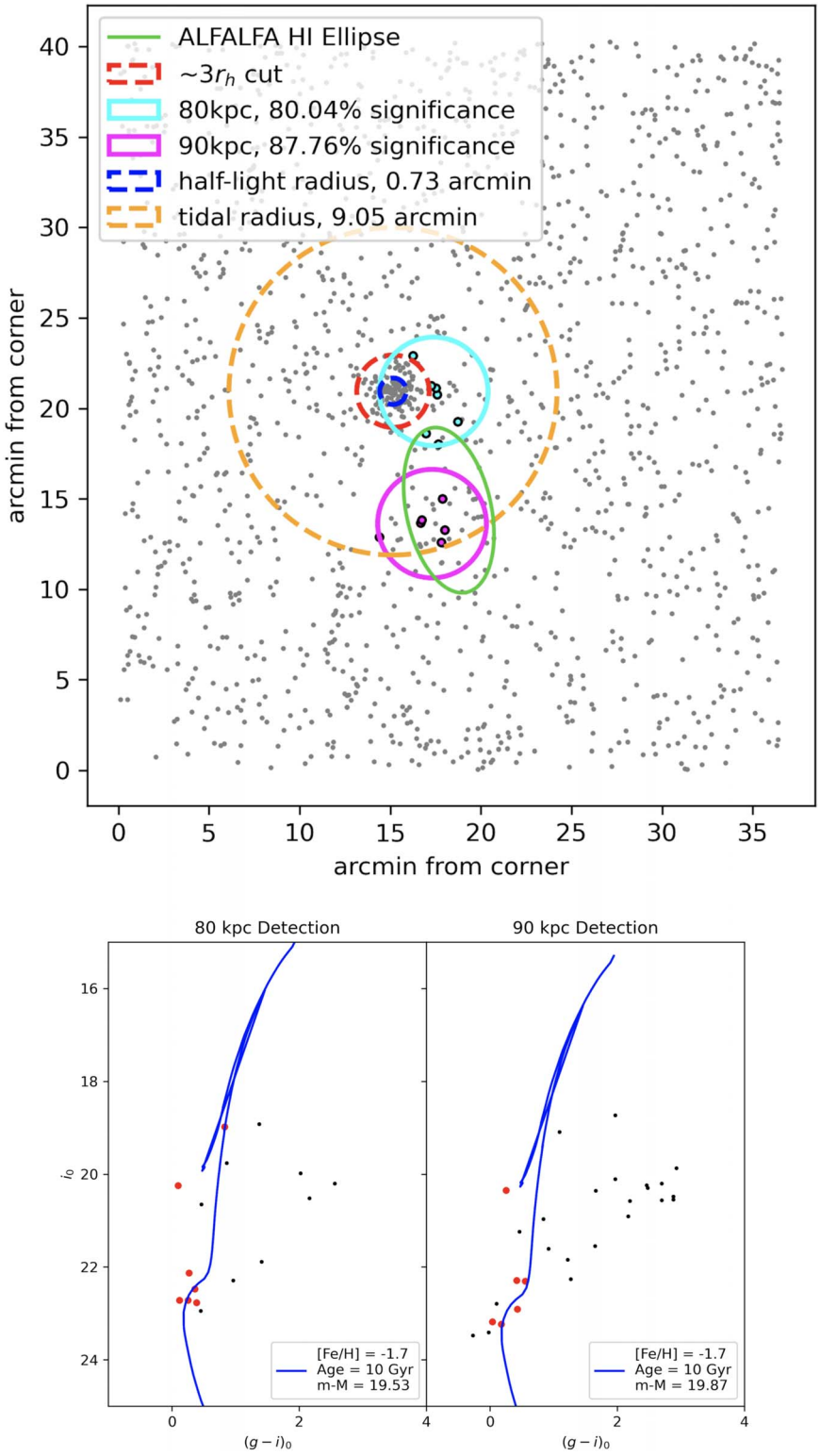

Figure 3. Top: diagram showing the positions of sources across the FOV of our ODI images of AGC 501816, which includes the Galactic GC Pal 3. Gray points mark the locations of objects in the final stellar catalog (after cross-matching with the Gaia EDR3 and SDSS catalogs and removing contaminants). The ALFALFA H I source is shown with a solid green ellipse. Pal 3 is the cluster of point sources ∼7 arc minutes away from the H I centroid. The half-light radius and tidal radius of the GC from Baumgardt & Hilker (2018) are marked, along with the 3 r_h circle used to remove Pal 3 stars before we searched for stellar overdensities associated with the H I. Two detected overdensities are marked with cyan and purple circles. The stellar overdensities and the H I source are either inside or overlapping with the tidal radius of Pal 3. Bottom: the CMDs for the two stellar overdensities detected in the AGC 501816 field after all stars within 3 r_h of Pal 3's center were removed. Gray points are all sources inside a 3′ radius around the peak of the overdensity, and red points are sources within that radius that fall within the CMD filter at the given distance. For reference, we have overplotted an isochrone from Girardi et al. (2004; solid blue line) with the age and metallicity of Pal 3 (10 Gyr, [Fe/H] $= -1.7$ or $Z = 0.0004$; Hilker 2006), shifted to match the distance at which each overdensity is detected (80 kpc or 90 kpc).

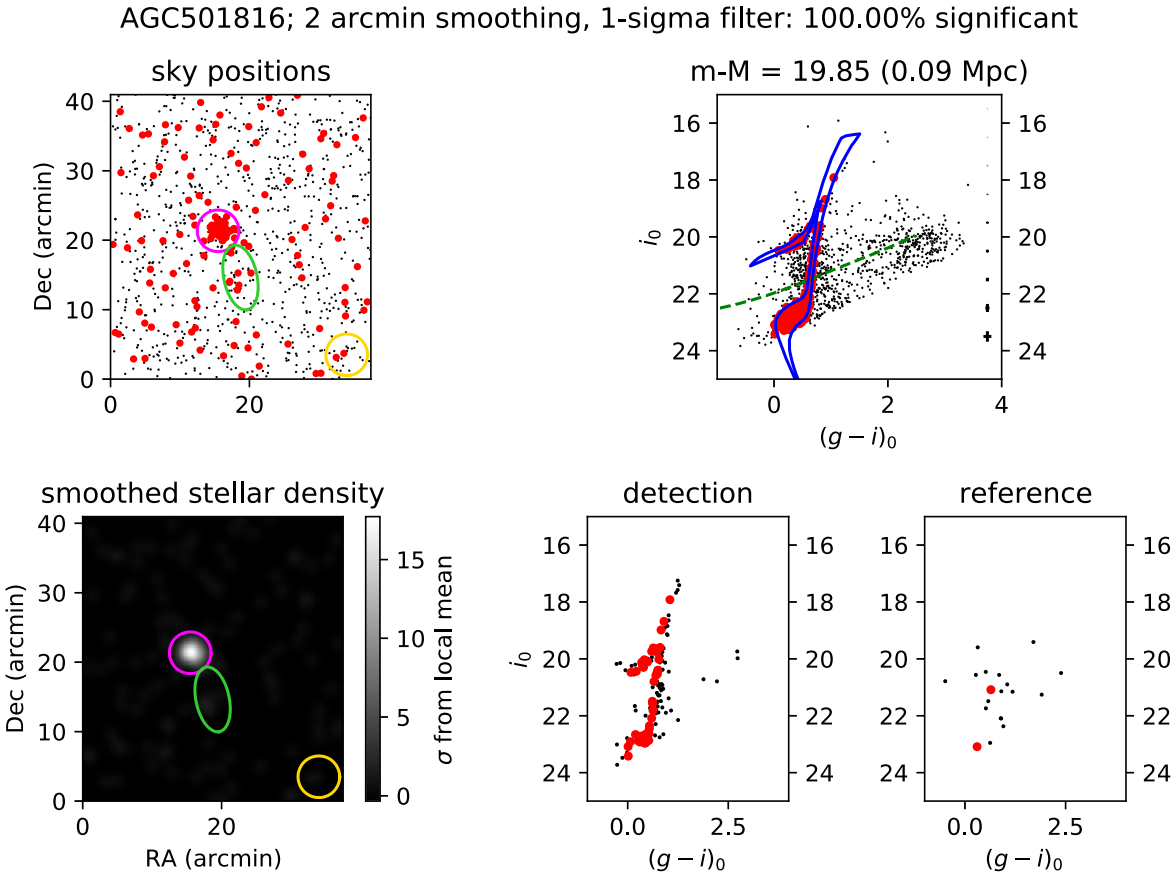

Figure 4. The UCHVC AGC 501816 is located on the sky roughly 7′ from the outer Galactic halo globular cluster Pal 3. We ran the detection pipeline on the images of the AGC 501816 field with Pal 3 present and with Pal 3 removed; this set of plots shows some of the results from the searches carried out with the GC present in the images. The top-left plot shows the locations of the stars detected in the field (gray points), the stars selected by the CMD filter (red points), and the H I ellipse for the UCHVC from ALFALFA (green ellipse). The region of the detected overdensity is marked with a magenta circle of radius 3′. A yellow circle of the same size is placed at a random location in the outskirts of the field and used to generate a comparison CMD; the sources within the detection and reference circle are compared as part of the assessment process described in Section 4.3. The plot on the bottom left shows the smoothed surface density map of the CMD-selected stars, with the same magenta and yellow circles and the green ellipse as are shown in the top-left plot. The CMD in the top right shows all of the sources in the field (black points), the CMD filter (blue solid line), and the CMD-selected stars (red points). The CMDs for objects located within the detection circle and comparison (reference) circle appear on the bottom right. The detection pipeline found Pal 3 at 100% significance at a distance range of 86−106 kpc, which brackets the actual distance of the cluster. It was also found at a distance of ∼160 kpc because of a combination of factors, including the shape of the CMD filter; see Section 5.1.2 for a full discussion.

provides a useful check of our methods for finding metal-poor, old stellar associations in our images, since it allows us to see how effectively the pipeline detects the Pal 3 stars, and whether it finds them at the appropriate distance. The second approach allows us to carry out the usual search for stellar populations in a wide area around AGC 501816, as we had done with all of the other UCHVCs in the sample.

We first carried out the detection steps described in Section 4 with the Pal 3 stars in place. We used the same CMD filter as before, but we changed the lower limit of the distance range to 25 kpc (down from 250 kpc) in order to include Pal 3's much closer distance in our search process. Searching the field with the Pal 3 stars in place yielded multiple detections at the location of Pal 3 with high statistical significance (100%). The distances corresponding to this local maximum in significance ranged from 86–106 kpc, a distance range that encompasses the actual measured distance of Pal 3 (91.9 kpc). For the detections within this distance range, the stars selected by the CMD filter populated the RGB, HB, main-sequence turnoff (MSTO), and the upper main sequence. The stellar densities for these detections were more than 15 times the mean density across the field. Figure 4 shows a typical example of the detection results with the Pal 3 stars present in the images; in this example, the stellar overdensity is detected at a distance of ∼93 kpc.

The pipeline also detected the Pal 3 stars at high significance (100%) at a distance of ∼160 kpc. A close examination of the results shows that this is caused by a combination of factors: the distance range being sampled, the shape of the lower portion of the CMD filter, and the detection limits of our data. When we use the CMD filter to search for stellar populations at close distances—i.e., between ∼25 and ∼150 kpc—the MSTO portion of the filter is included in the filtering process. This portion of the filter is wide compared to the other CMD features and allows stars with a broader range of magnitudes and colors to be selected. At nearby distances, the position of the MSTO feature also coincides with regions of the CMD where our photometric errors are larger (i.e., at i magnitudes between ∼22−24). The end result is likely that a higher level of contamination exists in the sample of filter-selected stars. The strong detection at 160 kpc occurred because that is the point at which the broad MSTO feature in the filter falls just *below* the typical detection limits of our data, and therefore only stars that coincide with the narrower RGB and HB portions of the filter are selected. This lowers the mean surface density of stars selected across the field and allows the bright

stars in Pal 3 that intersect other parts of the filter to yield a strong detection with a high surface density relative to the mean density in the field. This type of false detection should not occur in any of our other searches, because we normally only sample the distance range 250 kpc to 2.5 Mpc, which means that the MSTO feature is well below our detection limits. The bottom line is that the results of the search carried out with the Pal 3 stars in place confirms that our detection method can easily find a genuine old, metal-poor stellar population present in the images and that it yields a strong detection at the correct distance.

We next removed Pal 3 by excluding stars within 3 r_h of the cluster center in order to search for stars that might be associated with the H I source a few arcminutes away. A few overdensities with high significance ($\gtrsim$90%) were identified, so we carried out the final set of detection steps—i.e., cross-matching the CMD-filtered source list with Gaia and SDSS to remove likely contaminants and then repeating the detection process on the more restricted catalog. The process yielded two possible stellar overdensities, both of which are marked in the map of the field in Figure 3. One detection, with a final significance of 87.76%, closely coincides with the H I centroid and is found at a distance of ∼90 kpc. The detection is made up of only six stars that lie in the MS turnoff portion of the CMD filter, which is the broadest part of the filter and also (at the relevant distance) falls well below the 50% detection limit of our images. A second detection has a statistical significance of only 80.04% and is made up of only seven stars, but is worth mentioning because it is located very close to Pal 3, and is well inside the tidal radius of the cluster. Five of the seven stars lie in the MSTO region of the CMD filter and the others coincide with the HB and lower RGB. The distance yielded by the CMD filter for this object is ∼80 kpc.

The locations of the two detected overdensities are marked in the diagram of the field presented in Figure 3. The CMDs for the sources that make up the overdensities are shown in the bottom panels of that figure. For reference, a single isochrone with the age and metallicity of Pal 3 is plotted on each CMD, shifted to the distance at which the stellar overdensity is detected.

The question that arises at this point is what these two modestly significant detections might represent. One clear possibility is that the detected stellar overdensities are not genuine stellar populations associated with Pal 3 or AGC 501816 but are instead simply chance superpositions of stars that happen to have magnitudes and colors that fall within the CMD filter at the given distances. Another option is that we have detected stars that are somehow associated with Pal 3, with the H I source, or with both objects. The latter might be possible if, for example, the H I and stars originated in Pal 3 and then were subsequently removed somehow from the cluster, or the gas was stripped first and then stars formed within it later.

Evidence that argues against the idea that the gas could have been stripped from Pal 3 is that if the H I were at the same distance as Pal 3 and the detected overdensities (∼80−90 kpc), the mass of AGC 501816 (based on combining the ALFALFA flux S_{21} with the distance using Equation 7 in Adams et al. 2013) would be $\sim 2-3-10^3\ M_\odot$. This is a substantial amount of H I gas to have originated in a globular cluster, especially since it is found at a projected separation of ∼7′, or ∼180 pc at a distance of 90 kpc. Most other studies have estimated gas masses on the order of tens of $M_\odot$ or less for globular clusters. Another issue is that the gas appears at a velocity that makes it difficult to distinguish from Galactic neutral hydrogen. As mentioned, the H I source was included in the UCHVC sample slated for optical follow-up because of its other properties and its proximity to Pal 3, and despite the fact that its $|v_{\rm LSR}|$ value, 99 km s^{-1}, is lower than the 120 km s^{-1} minimum threshold. The ALFALFA detection grid in the vicinity of AGC 501816 and Pal 3 shows strong, widespread Galactic H I emission primarily at substantially lower velocities, but also shows a modest amount of weak, diffuse Galactic emission in the velocity range ∼100−125 km s^{-1}; thus we cannot be certain that AGC 501816 is not gas associated with the Milky Way. We conclude that additional observations of both the H I and the optical sources in the field around Pal 3 and AGC 501816 are needed in order to definitively determine whether or not there is any connection between these two objects.

5.1.3. Five Objects Classified as "Possible Detections"

Five of the UCHVCs we analyzed in the sample of 26 yielded stellar overdensity detections that we categorize as "possible detections" because they are only modestly convincing, but may warrant future follow-up observations. These five detections survived all of the analysis steps, including the cross-matching step with the Gaia and SDSS catalogs, and still met our criteria for identifying possible dwarf galaxy candidates. However, they were only significant in one of the two smoothing kernels (in all cases, the 2′ kernel), and some of their other properties suggest they may not be genuine stellar counterparts to the UCHVCs. Figure 5 shows the CMDs and spatial locations of the sources in the fields of each of the five UCHVCs, and Table 3 provides information about the detected stellar overdensity, including the significance, estimated distance, the sky coordinates, the log of the H I gas mass (if the UCHVC were at the same distance as the detected overdensity), the estimated M_V and stellar mass of the stellar counterpart (the calculation of these quantities is described in Section 5.2), and the estimated ratio of the atomic gas mass to the stellar mass ($M_{\rm HI}/M_*$). Details about each of these five objects are provided below.

AGC 115710:— This field yielded the stellar overdensity that had both the highest significance (99.55%) and the closest CMD filter distance (270 kpc). The CMD filter includes several bright objects that might be suitable targets for follow-up spectroscopy. On the other hand, the overdensity is relatively far from the H I centroid (7.′4 or ∼580 pc in projection), and a few background galaxies appear in the area around the overdensity.

AGC 122835.— This UCHVC field yielded an overdensity with one of the highest levels of significance, 95.30%. The same overdensity was detected both before and after the catalog cross-matching step, and even increased in significance between the two iterations. The distance to the stellar overdensity (based on the location of the CMD filter) is estimated at 870 kpc, and the projected separation from the H I centroid is 4.′5, which corresponds to a physical separation of 1.1 kpc at the 870 kpc distance. The stars in the detected overdensity do a fair job of filling in the RGB region of the CMD filter, from the top of the RGB down to the faint limits of the images. On the other hand, the CMD of the sources in the reference circle looks similar, both in terms of the number of stars and their locations in the color–magnitude plane.

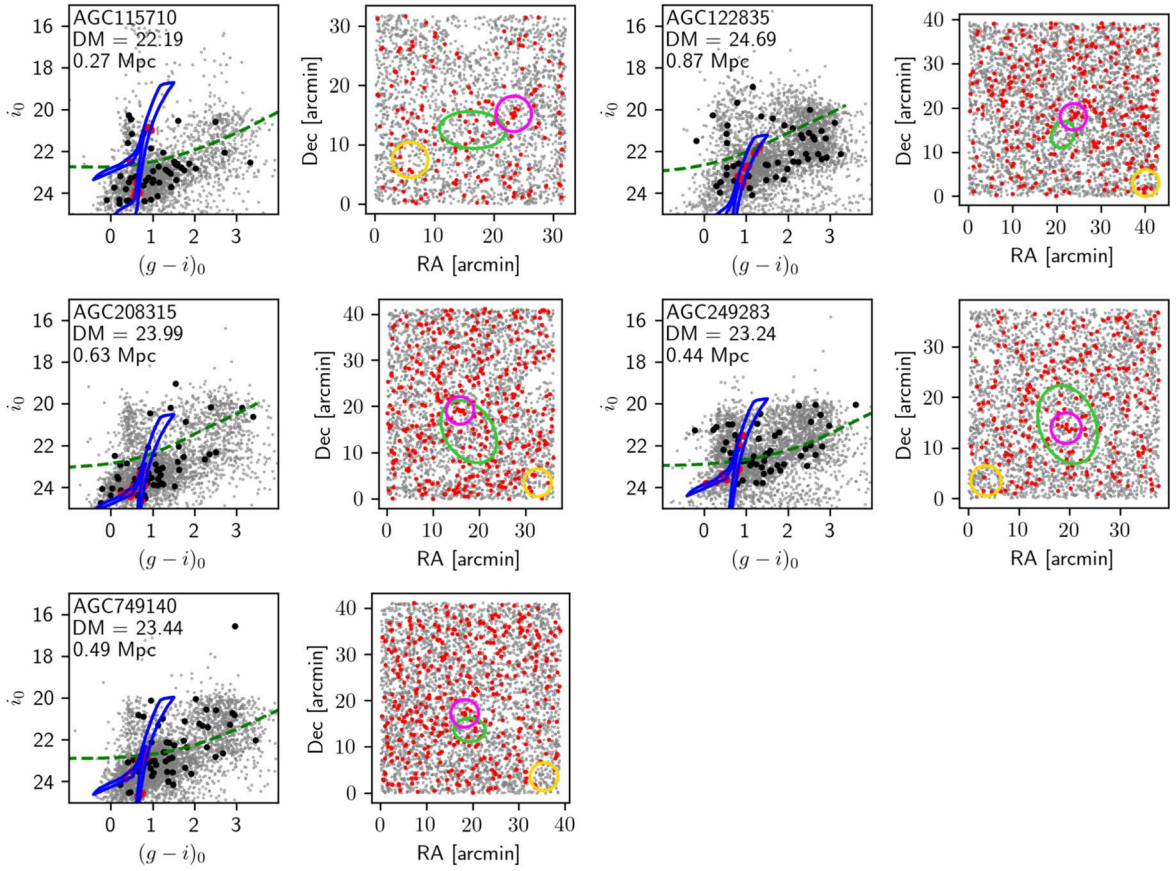

Figure 5. The CMDs and spatial positions of the point sources detected in the images of five UCHVCs classified as "possible detections." The UCHVC name appears in the top-left corner of the CMD. Each CMD shows the location of the filter (blue solid line), the distance modulus and distance of the detected stellar overdensity, and the 50% completeness level (green dashed line). In the CMDs, the gray points are the point sources that survive cross-matching with Gaia and SDSS, sources within 3′ of the overdensity peak are plotted in black, and sources that also fall within the CMD filter are overplotted in red. In the spatial position plots, the gray points are point sources that survive cross-matching with Gaia and SDSS, and red points are sources that are selected by the CMD filter. Also marked are the overdensity peak (magenta circle of 3′ radius), the H I ellipse (green), and the reference circle (yellow).

AGC 208315.— The stellar overdensity detected near this UCHVC is only modestly significant (86.87%) and has an estimated distance of 630 kpc. It is located approximately 4.′9 (∼900 pc) in projection from the H I centroid but nevertheless lies almost entirely within the H I ellipse (Figure 5). A small collection of stars is readily visible in the spatial plot, and the region within the detection circle is more populated than the region within the reference circle. However, the stars that make up the overdensity do not fill in the RGB region of the CMD filter, and all of them fall below the 50% completeness line in the CMD.

AGC 249283.— The stellar overdensity associated with this UCHVC is of interest mainly because it lies directly on top of the H I cloud, with a projected separation from the H I centroid of 0.′8. This translates to ∼100 pc at the estimated distance given by the CMD filter, which is 440 kpc. The stars that make up the overdensity lie within both the RGB and HB regions of the CMD filter, and the detection circle is clearly more populated than the reference circle. The major drawback of this detection is its lower significance, which decreased from ∼88% to 83.13% after the catalog-matching step.

AGC 749140.— The overdensity detected in this field has a significance of 93.04% and a CMD filter distance of 490 kpc, and became the prevalent detection after the cross-matching step. It is about 3.′7 (527 pc) from the H I centroid. The stars within the overdensity do appear more clustered than the stars in the surrounding image; however, none of the stars in the CMD filter are bright, and the detection is due to the presence of objects in the lower part of the RGB only, where the photometric uncertainties begin to increase.

5.1.4. Object Classified as the "Best Detection"

The images of the UCHVC AGC268071 yielded the most convincing dwarf galaxy candidate identified in the ODI imaging data; this object falls in the "best detection" category. The initial run of the detection pipeline on the ODI images of AGC 268071 yielded possible detections of an optical counterpart at a range of distances with statistical significance above 90%, so we carried out the catalog cross-matching steps and then searched with the more restricted catalog. The end result was a detection of a stellar association with high statistical significance that is located 9.′2 from the H I centroid. The same detection appears at 95.7% significance when we use a 2′ smoothing kernel and at 97.3% significance when we use a 3′ kernel. The estimated distance for this putative dwarf galaxy counterpart is 570 kpc, with a possible range between 490 and 590 kpc.

The diagram showing the results (including the CMDs for the field, the spatial locations of the stars relative to the H I, and the smoothed stellar distribution) for the 3′ smoothing kernel is shown in Figure 6. The stellar overdensity detected with the 3′ smoothing kernel includes 11 stars that are noticeably clustered

Table 3
Stellar Overdensities Found in the UCHVC Images Analyzed for This Work

Name	Significance (No. stars) (%)	Distance[a] (Range) (Mpc)	R.A.	Decl.	log $M_{\rm HI}$ ($M_\odot$)	M_V (Faint) (mag)	M_V (Bright) (mag)	g–i (Faint) (mag)	g–i (Bright) (mag)	log M_* (Faint) ($M_\odot$)	log M_* (Bright) ($M_\odot$)	$M_{\rm HI}/M_*$ (Faint)	$M_{\rm HI}/M_*$ (Bright)
Possible Detections													
AGC115710	99.55(9)	0.27 (0.25–0.31)	01:25:53.7	+05:25:51.3	$4.93^{+0.11}_{-0.08}$	$-2.18^{+0.19}_{-0.27}$	$-7.01^{+0.19}_{-0.27}$	0.92 ± 0.02	1.19 ± 0.01	$3.22^{+0.11}_{-0.08}$	$5.35^{+0.11}_{-0.08}$	50.82 ± 0.12	0.38 ± 0.01
AGC122835	95.30(10)	0.87 (0.86-0.92)	02:05:26.0	+29:17:57.1	$5.34^{+0.05}_{-0.01}$	$-4.47^{+0.03}_{-0.12}$	$-7.67^{+0.03}_{-0.12}$	1.57 ± 0.03	1.49 ± 0.07	$4.62^{+0.05}_{-0.01}$	$5.50^{+0.05}_{-0.01}$	5.17 ± 0.01	0.69 ± 0.01
AGC208315	86.87(12)	0.63 (0.59-0.64)	10:27:08.8	+08:51:41.2	$5.67^{+0.02}_{-0.01}$	$-3.63^{+0.14}_{-0.04}$	$-6.97^{+0.14}_{-0.04}$	0.26 ± 0.03	0.63 ± 0.08	$3.30^{+0.02}_{-0.05}$	$4.78^{+0.02}_{-0.05}$	232.23 ± 0.54	7.74 ± 0.02
AGC249283	83.13(9)	0.44 (0.42-0.50)	14:23:58.7	+05:22:56.6	$4.72^{+0.10}_{-0.04}$	$-3.52^{+0.11}_{-0.24}$	$-8.15^{+0.11}_{-0.24}$	1.41 ± 0.02	1.59 ± 0.05	$4.13^{+0.10}_{-0.04}$	$5.74^{+0.10}_{-0.04}$	3.91 ± 0.01	0.09 ± 0.01
AGC749140	93.04(9)	0.49 (0.43-0.49)	00:51:20.7	+15:14:46.3	$4.88^{+0.01}_{-0.11}$	$-3.18^{+0.27}_{-0.02}$	$-6.92^{+0.27}_{-0.02}$	0.84 ± 0.03	0.94 ± 0.05	$3.56^{+0.01}_{-0.11}$	$5.13^{+0.01}_{-0.11}$	20.64 ± 0.10	0.56 ± 0.01
Best Detection													
AGC268071	97.30(11)	0.57(0.49-0.59)	16:12:55.6	+14:20:45.3	$5.31^{+0.04}_{-0.13}$	$-4.29^{+0.32}_{-0.10}$	$-6.99^{+0.32}_{-0.10}$	1.12 ± 0.01	1.03 ± 0.01	$4.21^{+0.04}_{-0.13}$	$5.31^{+0.04}_{-0.13}$	12.48 ± 0.03	1.21 ± 0.01

Note.
[a] The distance listed here is the CMD filter distance associated with the most significant detection of a given overdensity. The numbers within the parentheses represent the range of distances for which a given detection remains above some significance threshold (90% for overdensities that have a peak significance $\geqslant$ 90%, and 80% for overdensities with a peak significance between 80% and 90%.).

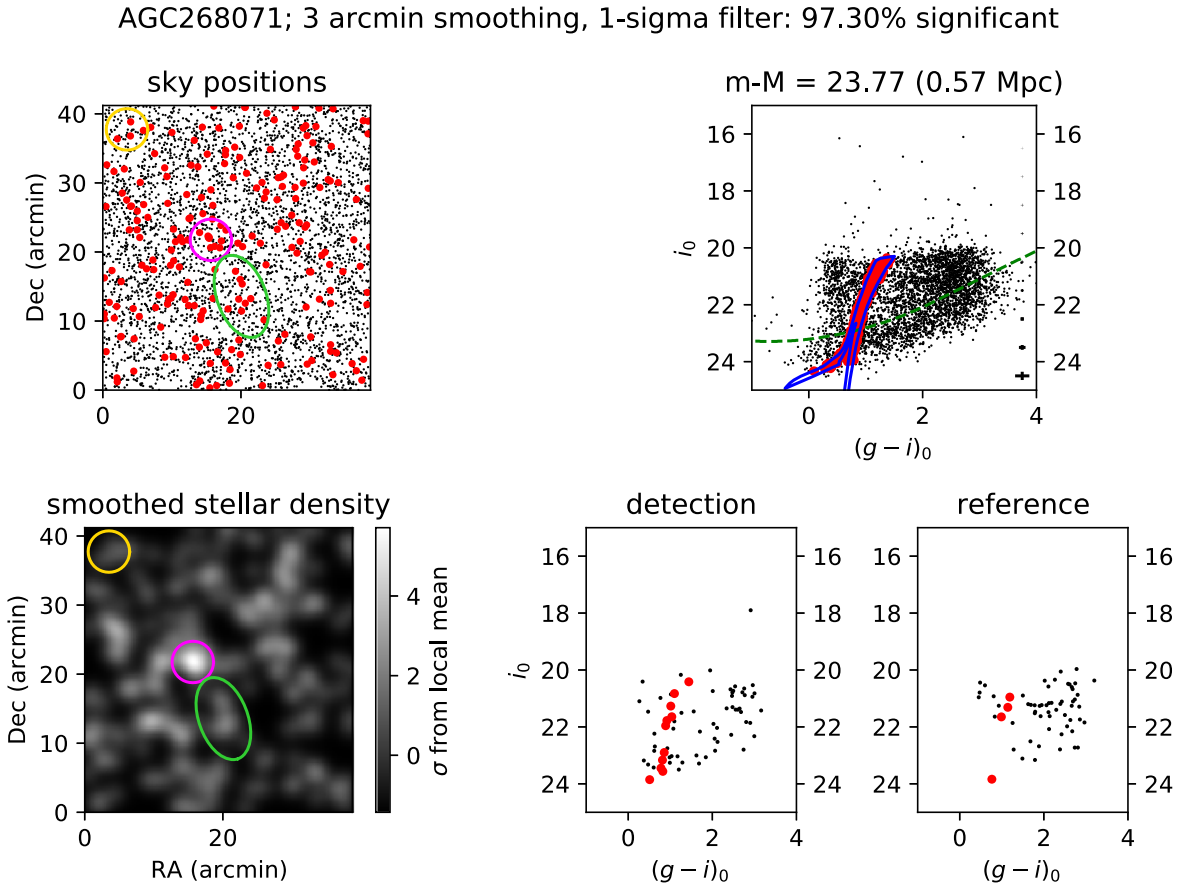

Figure 6. CMDs and spatial positions of the point sources detected in the images of the UCHVC AGC 268071. A stellar overdensity with a statistical significance of 97.30% is detected ∼9′ from the centroid of the H i source. The top-left plot shows the locations of the stars detected in the field (gray points), the stars selected by the CMD filter (red points), the H i ellipse from ALFALFA (green ellipse), the 3′ radius detection circle (magenta), and a reference circle of the same size placed at a random location in the outskirts of the field. The smoothed surface density map of the CMD-filtered stars is shown on the bottom left, with the detection and reference circles and H i ellipse marked as in the top-left plot. The CMD in the top right shows all of the sources in the field (black points), the CMD filter (blue solid line), and the CMD-selected stars (red points). The CMDs for objects located with the detection circle and comparison (reference) circle appear on the bottom right.

in the spatial distribution on the sky and that populate the RGB portion of the CMD filter reasonably well. Furthermore, there are appreciably more stars in the detection circle (11 stars) compared to a reference circle (four stars) of the same size placed at a random position within the field (bottom-right panel of Figure 6). On the other hand, there are a few background galaxies that appear in the ODI image in the general area of the overdensity, so it is certainly possible that the detection is at least partially due to the presence of a collection of unresolved background galaxies that happen to have magnitudes and colors that fall within the CMD filter. Also concerning is the fact that the stellar overdensity is located relatively far away from the H I centroid; at a distance of 570 kpc, the 9.′2 angular separation between the stellar overdensity and the H I translates to a projected physical separation of 1.5 kpc. It may be worth noting that AGC 268071 has the largest W_{50} value of any of the UCHVCs included in our sample (Table 1) and in the UCHVCs catalog published in Adams et al. (2013). Follow-up spectroscopy of some of the stars in the detected overdensity would be useful for determining whether the sources are genuinely associated with the H I source found by ALFALFA, or are simply the result of a random clustering of foreground and background objects. This would be challenging because the detection CMD in Figure 6 shows that the stars in the detected overdensity are faint, with the brightest having an i magnitude of 20.4 mag.

5.2. Estimating the Optical Properties of the Candidate Stellar Populations

We can utilize the information provided by the ODI imaging data to calculate rough estimates of the optical brightness of the potential stellar populations we have detected. For completeness, we carry out this calculation for all six of the sources in the current sample that we classify as either "possible detections" or the "best detection." We calculate two estimates of the photometric properties of the detected stellar overdensities and combine those with the estimated distance to produce a faint and bright limit for the magnitude of the dwarf galaxy candidate that may be associated with the H I.

To calculate the faint estimate, we simply combine the flux from each of the CMD-selected stars that make up the overdensity. This is a conservative estimate of the brightness and assumes that these are the only stars associated with the H I (i.e., that there is no underlying fainter stellar population present).

To arrive at a bright limit for the magnitude of the possible stellar population, we carry out aperture photometry of the images at the location of the stellar overdensity. First we mask out bright objects that are not part of the detected overdensity (e.g., extended background galaxies and stars that are much brighter than the CMD-selected stars) as well as background pixels that deviate appreciably from the median sky

Table 4
UCHVCs from J19 That Were Reanalyzed for This Study

Name	R.A.	Decl.	S_{21} (Jy km s^{-1})	cz (km s^{-1})	w_{50} (km s^{-1})	$\bar{a}$ ($'$)	log $\bar{N}_{HI}$ (atoms cm^{-2})	log M^{a}_{HI} ($M_{\odot}$)	Obs. Date	Detection
AGC198606	$09^{h}30^{m}05\overset{s}{.}5$	$+16^{d}39^{m}03^{s}$	6.73 ± 0.67	53	21 ± 1	9.00	19.60	6.20	2013A	ND
AGC215417	$11^{h}40^{m}08\overset{s}{.}1$	$+15^{d}06^{m}44^{s}$	0.70 ± 0.07	216	17 ± 4	9.49	18.50	5.20	2013A	ND
AGC219656	$11^{h}51^{m}24\overset{s}{.}3$	$+20^{d}32^{m}20^{s}$	0.85 ± 0.08	192	21 ± 1	8.00	18.80	5.30	2013A	ND
AGC249525	$14^{h}17^{m}50\overset{s}{.}1$	$+17^{d}32^{m}52^{s}$	6.73 ± 0.67	48	24 ± 7	9.00	19.60	6.20	2013A	BD
AGC268069	$16^{h}05^{m}32\overset{s}{.}6$	$+14^{d}59^{m}20^{s}$	1.14 ± 0.11	132	29 ± 4	7.07	19.00	5.40	2013A	ND

Note. Following Haynes et al. (2018), the adopted error on the recessional velocities listed in column 5 is half of the w_{50} error. The H I mass values in column 9 are calculated at an assumed distance of 1 Mpc. In the "Detection Status" column, objects for which no detection in the field meets our lower-threshold criteria are listed as "ND," and objects with our best (most convincing) detections are listed as "BD"; see Section 4.3 for more information about the categories.

background level in that part of the image. We replace the masked pixels with the median sky value and then measure the flux in the region of the overdensity. We set our aperture size to be based on the apparent angular size of the nearby dwarf galaxy Leo T (Irwin et al. 2007) if it were located at the physical distance of our detection. Therefore, the aperture ranges in size from roughly $1\farcm4$–$4'$ in diameter, given the range of estimated distances of the detected stellar overdensities (Table 3).

We also calculate a g–i color that corresponds to the faint and bright estimates, by subtracting the faint i magnitude from the faint g magnitude, and doing the same thing for the bright magnitudes. We use the computed g, i magnitudes and colors, the estimated distance, and the photometric conversion relations in Jester et al. (2005) to calculate the total absolute magnitude in the Johnson V filter, M_V.

We can combine these magnitude and color estimates to calculate at least an approximate stellar mass range for the candidate stellar populations we have identified. We combine the relations in Bell et al. (2003) with our magnitudes and colors to estimate the possible range of mass-to-light ratios for each object and then apply those values to the faint and bright magnitude limits to calculate the range of stellar masses. We also calculate the ratio of the H I mass to the stellar mass for the faint and bright cases.

The optical magnitude and color estimates, and the associated H I mass to stellar light ratios, are included in Table 3. The faint and bright estimates for a given object can vary from each other by a few magnitudes, which means the optical brightness of the putative stellar counterparts are highly uncertain. Nevertheless, having at least a rough estimate allows us to compare the properties of these objects to the properties of simulated and observed dwarf galaxies in the Local Group (see Sections 6.2.2 and 6.2.3).

5.3. Revisiting the Stellar Overdensities Identified in the UCHVC Sample from J19

Because of the improvements we had made to the stellar overdensity search process, it seemed appropriate to reprocess and reassess the five potential stellar overdensities that were detected in the J19 sample. We carried out a full analysis of the imaging data for those five objects, beginning with running source detection and photometry on the combined g and i image pairs and proceeding all the way through the Gaia and SDSS catalog cross-matching steps and the final assessment of the results. Information about the five UCHVCs that were reanalyzed in this way is listed in Table 4; the table columns are the same as those in the corresponding tables for the primary sample of UCHVCs (Tables 1 and 2).

After processing and analyzing these objects with the updated procedures, we found that four out of the five possible overdensities identified by J19 no longer had convincing detections. Although there were a few cases where a stellar overdensity with a significance of ∼80%−90% or above was found somewhere in the images, further scrutiny showed that in all cases the overdensity was too far away from the H I source, and/or the CMD of the stars within the detection circle looked too much like the CMD of the stars in the reference circle. Accordingly, we now categorize these objects as nondetections and mark them as "ND" in Table 4. Our overall conclusion is that the changes to the detection pipeline described in Section 4.5—especially the reduction in foreground and background objects from our star lists made possible by the catalog cross-matching—resulted in a more stringent process, which in turn showed that four of the five most significant overdensities presented in J19 are not likely to be genuine dwarf galaxies.

One UCHVC field, however, yielded a highly statistically significant dwarf galaxy candidate that meets our criteria for a "best detection." The UCHVC is AGC 249525, and the corresponding optical counterpart was first highlighted in Janesh et al. (2017) and was one of the most convincing dwarf galaxy candidates identified in the full sample of objects presented in J19. Using our updated detection methods, we find a highly significant overdensity that matches the characteristics of the original detection.

AGC 249525 has an H I mass of $\sim 10^7\ M_{\odot}$ (see Table 4), a column density log(N_{HI}) of 19.60 atoms cm^{-2}, and an apparent H I major axis of $\sim 9'$. This source is one of the UCVHCs that was observed with the WSRT and the VLA and has therefore been mapped at higher resolution (Adams et al. 2016; Bralts-Kelly et al. 2020; Paine et al. 2020). Bralts-Kelly et al. (2020) analyzed the VLA observations of AGC 249525 and concluded that they show a velocity gradient that is indicative of rotation support, but that more work is necessary to draw firmer conclusions about the H I kinematics of this object.

The stellar overdensity detected with the earlier version of the pipeline and presented in Janesh et al. (2017) and Janesh et al. (2019) had a statistical significance of ∼98%. It was located well within the ALFALFA H I ellipse and was directly coincident with the highest-density contour in the H I synthesis maps from the WSRT presented in Adams et al. (2016). Janesh et al. (2017) reported a distance of 1.60 Mpc, with an error (which they estimated by determining the range of distances over which the significance stayed above 95%, for this object)

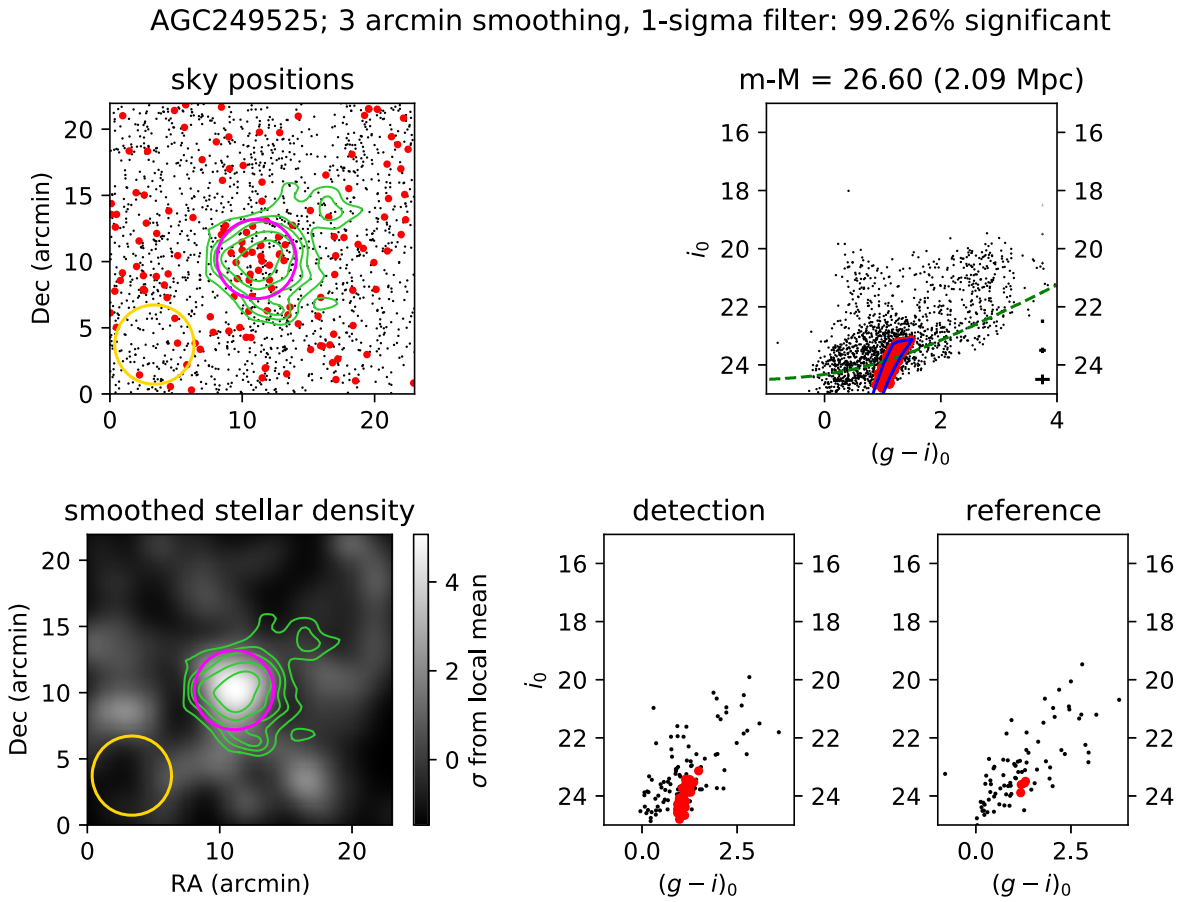

Figure 7. CMDs and spatial positions of the point sources detected in the images of the UCHVC AGC 249525, which was included in the sample presented in Janesh et al. (2019) and which we have reprocessed and analyzed with our updated detection pipeline. A stellar overdensity with a statistical significance of 99.26% is detected that coincides with the location of the H I source (green contours). The top-left plot shows the locations of the stars detected in the field (gray points), the stars selected by the CMD filter (red points), the 3′ radius detection circle (magenta), and a reference circle of the same size placed at a random location along the edges of the field. The smoothed surface density map of the CMD-filtered stars appears on the lower left, with the detection and reference circles marked in the same way as in the top-left plot. The CMD in the top right shows all of the sources in the field (black points), the CMD filter (blue solid line), and the CMD-selected stars (red points). The CMDs for objects located with the detection circle and comparison (reference) circle appear on the lower right. The H I contours from the Adams et al. (2016) WSRT study are shown with with green solid lines on the top-left and bottom-left spatial plots; the contour levels are [9, 15, 20, 30, and 40]–10^{18} atoms cm^{-2}.

of ± 0.45 Mpc. Their estimated stellar mass for the optical counterpart was between ∼2–10^4 and 4–10^5 $M_\odot$.

Our updated analysis yields a possible stellar counterpart at the same location as that found by Janesh et al. (2017), but with an increased statistical significance of 99.26%. The range of distances over which the detected overdensity has a significance above 90% is 1.93−2.12 Mpc, and the highest significance corresponds to a distance of 2.09 Mpc. This distance is slightly larger than the J19 distance, but the two distance ranges overlap.

The overdensity found by the new analysis is made up of 25 point sources that are selected by the CMD filter and located within a region 3′ in radius. These 25 sources all fall within the upper portion of the RGB in the CMD filter (see Figure 7). The number of sources in this detected overdensity is more than twice the number of sources that make up the other overdensities in the sample of UCHVCs presented in the current paper (see Table 3). The H I contours from the WSRT observations presented in Adams et al. (2016) are overplotted on the spatial plots of the field that are shown in Figure 7; the position of the stellar overdensity found with the updated pipeline remains coincident with the H I contour with the highest $N_{\rm HI}$ value.

A distance of 2 Mpc is near the upper end of the distance range over which we search for stellar counterparts, and at these large distances, the upper portion of the RGB coincides with the region of the CMD where the photometric errors become larger, our detection completeness is lower, and it becomes more difficult to distinguish true point sources from extended background objects in our ground-based images. Therefore follow-up observations—deeper, higher-resolution imaging, and/or spectroscopy of the sources that make up the detection—are needed in order to explore whether this overdensity is a genuine stellar counterpart to the UCHVC or is simply a collection of foreground and/or background objects that happen to coincide with the H I and lie in the relevant portion of the CMD.

We carried out the steps described in Section 5.2 to estimate the optical properties and the distance-dependent H I properties of the possible stellar counterpart to AGC 249525; these are listed in Table 5. The V-band absolute magnitude for the stellar counterpart is estimated to be in the range −5.99 to −6.87 mag. As one might expect (since the analysis was carried out on the same images, and we find the overdensity at a similar distance), these brightness estimates overlap the original brightness range estimated in J19 (M_V = −4.5 to −7.1 mag).

Table 5
Stellar Overdensities Found in the Reanalyzed UCHVC Images from J19

Name	Significance (No. stars) (%)	Distance[a] (Range) (Mpc)	R.A.	Decl.	log $M_{\rm HI}$ ($M_\odot$)	M_V (Faint) (mag)	M_V (Bright) (mag)	g–i (Faint) (mag)	g–i (Bright) (mag)	log M_* (Faint) ($M_\odot$)	log M_* (Bright) ($M_\odot$)	$M_{\rm HI}/M_*$ (Faint)	$M_{\rm HI}/M_*$ (Bright)
AGC249525	99.26(25)	2.09 (1.93-2.12)	14:17:53.9	+17:32:46.0	$6.80^{+0.01}_{-0.03}$	$-5.99\ ^{+0.07}_{-0.03}$	$-6.87\ ^{+0.07}_{-0.03}$	0.96 ± 0.03	0.92 ± 0.02	$4.77^{+0.34}_{-0.38}$	$5.09^{+0.01}_{-0.05}$	106.40 ± 2.15	50.84 ± 0.54

Note.
[a] The distance listed here is the CMD filter distance associated with the most significant detection of the overdensity. The numbers within the parentheses represent the range of distances for which the detection remains above 90% significance.

6. Summary and Discussion

6.1. Summary of Results

The UCHVCs investigated in this study were selected from the ALFALFA survey because they had relatively compact angular sizes, were isolated from other H I sources in both velocity space and location on the sky, had measured velocities that suggested they were within the Local Volume and were not likely to be Galactic H I, and did not have a clear optical counterpart in existing catalogs and survey data. Our goal was to determine whether any of the UCHVCs might actually host an as-yet undiscovered dwarf galaxy, perhaps even one like the dwarf galaxy Leo P, which was first identified as an ALFALFA UCHVC and then imaged in the optical with WIYN (Giovanelli et al. 2013; Rhode et al. 2013). If the UCHVCs do indeed host a dwarf galaxy, they would be some of the faintest, lowest-mass neutral-gas-bearing dwarf galaxies known in the nearby Universe, with absolute V-band magnitudes in the range ~ -2 to -8, stellar masses in the range $\sim 10^3$ to $10^6\ M_\odot$, but with a gas content in the range $\sim 10^5$ to $10^6\ M_\odot$ (for an assumed distance of 1 Mpc).

In the current paper, we have presented results from the second and final phase of our campaign to image a large sample of ALFALFA UCHVCs with WIYN. For this phase of the campaign, we made several improvements to our procedures for finding possible stellar counterparts to the H I clouds, and we analyzed high-quality g- and i-band imaging of 26 UCHVCs to look for dwarf galaxy candidates.

From the sample of 26 objects, we identified six UCHVCs with at least one significant detection. We also carried out a detailed analysis of ODI imaging of a UCHVC located a few arc minutes away from the Galactic outer halo GC Pal 3. Our best dwarf galaxy candidate is associated with the UCHVC AGC 268071; the stellar overdensity we identify has a statistical significance of 97.30%, a distance of ~570 kpc, and is located roughly 9′ (~1.5 kpc) from the centroid of the H I source.

We used our improved methods to reprocess and analyze the original WIYN imaging of the five UCHVCs from the first phase of the project that had possible stellar counterparts. From this set of five UCHVCs, we find one stellar counterpart that qualifies as a convincing detection based on our new procedures and criteria. The detected stellar overdensity appears at the same location and a similar distance (~2 Mpc) as the stellar overdensity originally identified in Janesh et al. (2017), but with an even higher statistical significance (99.3%) when compared to repeated experiments that randomly distribute the same number of stars around the field.

6.2. Putting Our Results in Context

6.2.1. Other Observational Searches for Dwarf Galaxy Counterparts to Compact H I Clouds

In the time since the discovery of Leo P, we have had only limited success at finding candidate dwarf galaxy counterparts to the UCHVCs selected from the ALFALFA survey data, and we have certainly found no counterparts that are as obviously apparent as Leo P. Leo P subtends roughly 90″ on the sky, has a total absolute V-band magnitude of $M_V \sim -9.3$, and has an underlying population of old (~12 Gyr) RGB stars, a young ($\leqslant$ 300 Myr) population of massive early-type stars, a prominent H II region (Rhode et al. 2013; McQuinn et al. 2015), and Hα emission that reveals the presence of extended (~100 pc) ring-like structures (Evans et al. 2019) in the galaxy's interstellar medium. Given its properties, Leo P was readily visible in our modest-length exposures (20−30 minute integrations in each of the B, V, and R filters) taken with WIYN (Rhode et al. 2013).

Other studies have looked for counterparts to H I sources identified in ALFALFA and other neutral hydrogen surveys and have also been met with limited or no success at finding Local Group dwarf galaxies, although they have identified new dwarf galaxies within the Local Volume and/or at Virgo Cluster distances. The survey that is most relevant to mention in this context is the Galactic Arecibo L-band Feed Array H I (GALFA-HI) survey. GALFA-HI was aimed primarily at studying the neutral hydrogen component of the Galactic interstellar medium (Peek et al. 2011), but in the process identified 27 clouds that were classified as "Galaxy candidates" because of their kinematics and separation from known galaxies or HVC complexes (Saul et al. 2012). Eleven of the ALFALFA UCHVCs from Adams et al. (2013) also appear in the GALFA-HI catalog.

Several groups carried out optical follow-up observations and archival imaging searches of objects chosen from the GALFA-HI and/or ALFALFA surveys. Bellazzini et al. (2015a, 2015b) used the Large Binocular Telescope to conduct the SECCO Survey, which obtained deep optical images of 25 of the ALFALFA UCHVCs. The survey resulted in the detection of a distant stellar counterpart to the UCHVC AGC 226067 that was dubbed SECCO 1 (Bellazzini et al. 2015b). Bellazzini et al. (2015a) suggested that the object was at least 3 Mpc away and was most likely a star-poor dwarf galaxy in the Virgo Cluster. Adams et al. (2015) subsequently published H I synthesis maps and optical imaging of AGC 226067 and its putative optical counterpart. Tollerud et al. (2015) used the WIYN pODI instrument to obtain follow-up imaging of 22 of the 27 GALFA-HI Galaxy Candidates from the list published by Saul et al. (2012). From this sample of 22 objects, Tollerud et al. (2015) identified two dwarf galaxies, dubbed Pisces A and Pisces B, that were visible in SDSS images and appeared to be nearby (at least within the Local Volume); they used spectroscopy with the Palomar 5 m to confirm that the dwarfs were genuinely associated with the H I. A subsequent HST imaging study by Tollerud et al. (2016) placed Pisces A and Pisces B at distances of 5.6 Mpc and 8.9 Mpc, respectively (we note that these objects were also cataloged by ALFALFA and designated AGC 103722 and AGC 114843; Haynes et al. 2018).

Sand et al. (2015) searched archival UV and optical data from a number of different surveys and facilities (DSS, SDSS, Subaru SMOKA, CFHT Megacam, GALEX, and Swift) to look for counterparts to a sample of UCHVCs selected from GALFA-HI and ALFALFA. They looked for blue, diffuse emission similar to the faint blue emission that was visible in the SDSS images of Leo P before its discovery (Giovanelli et al. 2013; Rhode et al. 2013). They identified six possible counterparts to their sample of UCHVCs and used spectroscopic follow-up to confirm that five of the counterparts were genuinely associated with the H I gas. All five of these counterparts are dwarf galaxies that lie outside the Local Group. Two of the dwarfs were the above-mentioned galaxies Pisces A and Pisces B from Tollerud et al. (2015). A third dwarf galaxy was SECCO 1, the object identified by Bellazzini et al. (2015b). Sand et al. (2017) followed up with an HST

study that showed that this object is ∼17 Mpc away and is likely a remnant dwarf galaxy produced through a ram pressure stripping event that occurred within the M86 subgroup of the Virgo Cluster. The remaining two dwarf galaxies found by Sand et al. (2015), GALFA Dw3 and GALFA Dw4, were observed with HST to confirm their location outside the Local Group (at 7.6 Mpc and 3.1 Mpc, respectively) and note their isolated nature (no other galaxies within 1.5 Mpc of either dwarf; Bennet et al. 2022).

Tollerud & Peek (2018) utilized the Exploring the Local Volume In Simulations (ELVIS) suite of simulations (Garrison-Kimmel et al. 2014) to create mock H I catalogs and explore how these compare to the results from GALFA-HI and the associated optical searches for Local Group dwarf galaxies. The ELVIS simulations were dark-matter-only simulations designed to model environments similar to the Local Group, with two massive galaxy halos in the same configuration (e.g., mass and position) as the dark matter halos that are thought to host M31 and the Milky Way. Tollerud & Peek (2018) utilized a simple empirical model to translate the dark-matter-only ELVIS simulations into GALFA-HI observables and then examine what the H I survey would be expected to find. Based on these mock catalogs, they found that they should potentially discover tens of Local Group dwarf galaxies (depending on the model), in contrast to the zero that were found in the actual observations. They argued that this discrepancy could be explained if reionization inhibited star formation at mass scales below the mass of galaxies like Leo T, which had an estimated virial mass at the time of reionization of $\sim 10^{8.5}\ M_{\odot}$.

The results shown in Tollerud & Peek (2018) were further investigated by DeFelippis et al. (2019), who combined the data in the GALFA-HI catalog with archival optical imaging data from the Panoramic Survey Telescope and Rapid Response System (Pan-STARRS; Chambers et al. 2016). DeFelippis et al. (2019) began by searching the GALFA-HI data for H I sources with the expected neutral gas properties of nearby dwarf galaxies and identifying 690 objects. They then applied a filtering technique to the Pan-STARRS archival data to look for stellar populations with a range of ages and metallicities that might be spatially associated with the H I. They also tested their algorithm by searching for, and successfully finding, known dwarf galaxies (namely, Leo T and Draco) at the appropriate distances. They found one potential dwarf galaxy candidate near the Galactic plane, but no objects that resemble Leo T, and argued that the results rule out the existence of Leo T-like objects within the GALFA footprint (which covers ∼one-third of the sky) at distances within 500 kpc. They conclude that their results support the Tollerud & Peek (2018) assertion that reionization caused the gas to be removed from Local Group objects with halo masses less than the $\sim 10^{8.5}\ M_{\odot}$ threshold, and thereby prevented those objects from developing into full-fledged dwarf galaxies.

6.2.2. Comparison of Our Results to Model Simulations

A useful next step for understanding our results in a larger context is to compare our most convincing dwarf galaxy candidates to the results from recent state-of-the-art simulations that attempt to model the formation of dwarf galaxies down to the lowest masses. Applebaum et al. (2021, hereafter A21) presented results from the DC Justice League suite of Milky Way−like zoom-in simulations, which were designed to probe galaxy formation down to the regime of ultra-faint dwarf galaxies (UFDs), i.e., down to absolute magnitudes of M_V fainter than −8 and stellar masses $\lesssim 10^5\ M_{\odot}$. The simulations were initially run to model large (∼50 Mpc across), dark-matter-only volumes and then small regions within those volumes were re-simulated at higher resolution with full hydrodynamical treatment. The smaller regions were specifically chosen to contain Milky Way analogs to enable meaningful comparisons between the simulation results and the observed properties of our local galaxy environment. Two Milky Way analogs, nicknamed "Elena" and "Sandra," with masses of $7.5–10^{11}\ M_{\odot}$ and $2.4–10^{12}\ M_{\odot}$, respectively, were selected for detailed simulations because they were isolated and had masses consistent with current observational estimates of the Milky Ways virial mass. The DC Justice League simulations included star and gas particles, feedback from supernovae and stellar winds, chemical evolution, star formation, and supermassive black hole formation and feedback. A21 cataloged the dwarf galaxies that were produced in each simulation and determined the satellite galaxies' stellar, gas, and virial masses, luminosities, half-light radii, metallicities, galactocentric distances, and star formation time scales. They were able to resolve UFDs with absolute magnitudes as faint as $M_V = -3$ and found that they could match the range of dynamical properties and size–luminosity scaling relations seen in the known Local Group dwarf galaxies down to scales of ∼200 pc. They also compared the properties of their simulated dwarf galaxies to the expected detection limits that the Legacy Survey of Space and Time (LSST) data from the Rubin Observatory will reach after 10 yr. They concluded that virtually all Local Group UFD galaxies will be detectable by LSST down to the luminosity limit probed by their simulations.

Because the DC Justice League simulations were able to produce dwarf galaxies with realistic properties, it should be instructive to compare the properties of their dwarf galaxies with the properties of the two most convincing dwarf galaxy candidates we identified in our search, namely the optical counterparts we find for the UCHVCs AGC 268071 and AGC 249525. We have recreated two of the figures from A21 that feature observable quantities that are also available for our dwarf galaxy candidates. In Figure 8, which is a recreation of Figure 5 from A21, we show the absolute *V*-band magnitudes of the simulated dwarf galaxies as a function of the distance to their parent galaxy normalized by the parent galaxy's virial radius. The figure makes it clear that the Sandra host galaxy was associated with many more satellite galaxies than the Elena host galaxy. A21 investigated this difference and attributed it to both the higher mass of the Sandra halo and to the fact that an analog to the Large Magellanic Cloud (which is associated with many of the ultra-faint dwarfs in the vicinity of the Milky Way) appears in the Sandra simulation but is not present in the Elena simulation. The simulated galaxies are also separated into three categories: satellite galaxies that are within the virial radius of their parent galaxy, field galaxies that are outside the virial radius of the parent, and "backsplash" galaxies that are field galaxies that have experienced an infall that has brought them within their parent galaxy's virial radius.

We have added our two dwarf galaxy candidates to Figure 8. To include them in the plot, we calculated the distances of the two dwarf galaxy candidates in terms of virial radius of the Milky Way (200 kpc; Dehnen et al. 2006). In the figure, AGC 268071 appears to fit within the population of field galaxies, which follow a weak trend of having fainter absolute

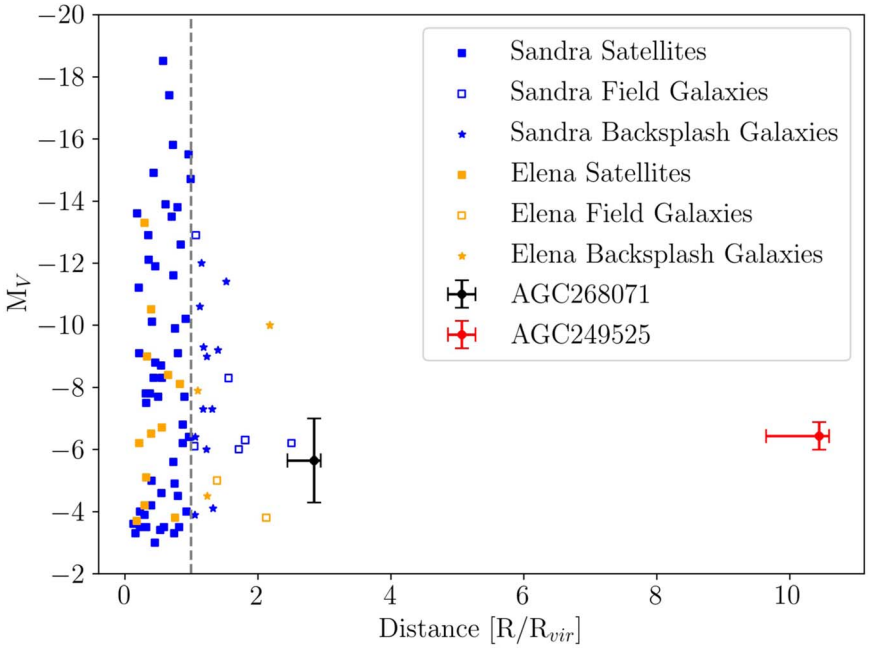

Figure 8. A recreation of Figure 5 from Applebaum et al. (2021), which shows *V* magnitude as a function of normalized distance for the dwarf galaxies in the Sandra and Elena simulations (blue and orange points, respectively). The dwarf galaxy candidates associated with the UCHVCs AGC 268071 and AGC 249525 are plotted on the figure (points with large error bars) for comparison. For both simulations, satellites are denoted with filled squares, field galaxies are shown as open squares, and backsplash galaxies are denoted with a star. For the optical counterparts to AGC268071 and AGC 249525, we plot the average of the ratios calculated from the bright and faint estimates of their photometric properties and use both estimates to bracket our uncertainty. The distance uncertainty for these two objects is determined by the distance over which each object is detected in our data (see Table 3). We note that the error bars representing the distance uncertainties for our dwarf galaxy candidates are not symmetric in this plot and in Figure 9 and 10. This reflects the fact that the significance of a given overdensity falls below the 90% or 80% threshold relatively quickly after the peak significance is reached, as the tip of the RGB in the CMD filter is shifted downward to fainter magnitudes and the handful of stars that make up a typical detected overdensity become too bright to coincide with the filter.

magnitudes with increasing distance from the parent galaxy. One of the simulated field galaxies that is produced in the Sandra simulation has properties that overlap those of AGC 268071, given the uncertainties on our estimated absolute magnitude and distance for this dwarf galaxy candidate. We include AGC 249525 for completeness, although it lies in a region that is not populated with the dwarf galaxies included in the simulation; it has an estimated absolute magnitude that is similar to those of AGC 268071 and the other field dwarf galaxies, but a distance that corresponds to more than 10 times the virial radius of the Milky Way.

In Figure 9, we present a similar figure to Figure 13 in A21, and show the H I-to-stellar mass ratios of the gas-bearing dwarf galaxies that appear in the Sandra and Elena simulations. Only the galaxies that A21 determined to have retained their gas (i.e., those that are not classified as "quenched" in their paper) are included in our version of the figure. The ratios are shown as a function of the distance (again normalized by the virial radius) from the parent galaxy. We also show the locations of the dwarf galaxy candidates we detect in the images of the UCHVCs AGC 249525 and AGC 268071. Many of the dwarf galaxies produced by the DC Justice League simulations do not have any neutral gas and therefore are not plotted. The dwarf galaxy candidate associated with AGC 268071 exists much farther out in distance from the parent galaxy than the majority of the simulated dwarfs and lies on the high end of the range of H I-to-stellar mass ratios. The dwarf galaxy candidate corresponding to AGC 249525 is even more extreme, in terms of both gas-to-stellar ratio and distance from the massive galaxy. Both dwarf candidates appear generally consistent with a mild trend for higher gas-to-stellar ratios with larger distances that is present in the simulated sample. The low stellar content (and/or high H I-to-stellar mass ratio) of the dwarfs at large distances may be at least partially explained by their isolated nature, as they would presumably be less subject to tidal effects from their parent galaxy or other nearby satellites and therefore perhaps less likely to either be stripped of their gas and/or to have undergone starbursts triggered by close interactions.

6.2.3. *Comparison of Our Results to the Population of Local Group Dwarf Galaxies*

In addition to comparing to simulated data, it is worthwhile to compare the dwarf galaxy candidates we detect to the actual dwarf galaxy population in and around the Local Group. In Figure 10, we plot the absolute *V*-band magnitude as a function of distance for dwarf galaxies within ∼3 Mpc. The values we show are taken from the sample included in McConnachie (2012), who compiled the measured properties (e.g., distances, magnitudes, metallicities, structural, and dynamical characteristics) of galaxies in the Local Group and its environs. In the figure, Milky Way satellite galaxies are shown in blue, M31 satellites are shown in orange, other nearby dwarf galaxies are shown in pink, and our dwarf galaxy candidates are shown in black and red. The positions of Leo T and Leo P are plotted with filled star symbols that are pink and gray, respectively. Since the other nearby dwarf galaxies are not bound to either the Milky Way or M31, we use their distance from the barycenter of the Local Group as the distance value on the *x*-axis of the figure, except that for Leo P we use the distance from McQuinn et al. (2015). For the counterparts to AGC 268071 and AGC 249525, we simply use the estimated

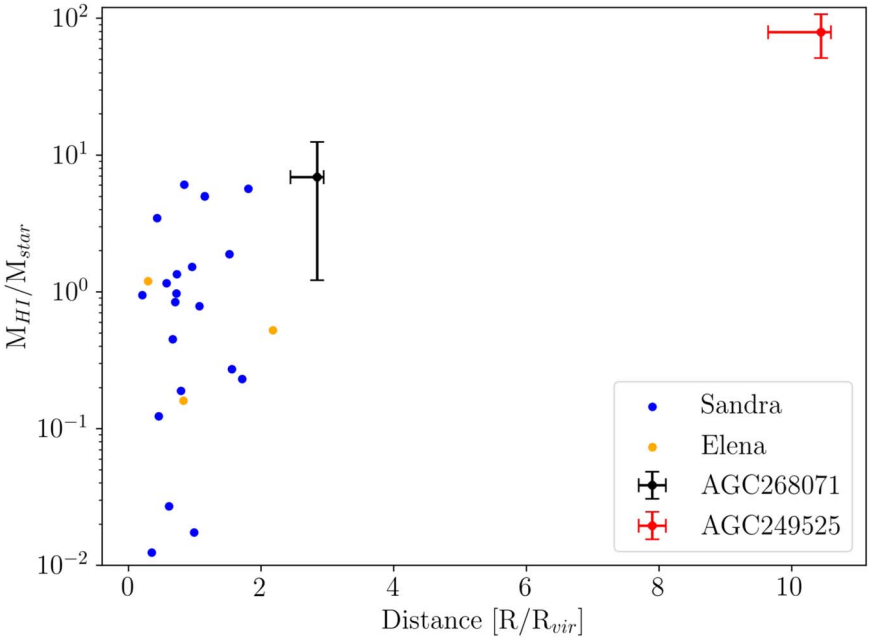

Figure 9. A recreation of Figure 13 from A21, which shows the H I-to-stellar mass ratio as a function of normalized distance from the parent galaxy for simulated dwarf satellite galaxies associated with Milky Way analogs. We have added the dwarf galaxy candidates we found that are associated with the UCHVCs AGC 268071 and AGC 249525. Blue points represent galaxies in the Sandra simulation, while orange points represent galaxies in the Elena simulation. Note that many of the galaxies in the simulations do not have H I gas and therefore are not plotted. For AGC 268071 and AGC 249525 (points with large error bars), we plot the average of the bright and faint magnitude estimates and use both estimates to set the uncertainty. The distance uncertainty for these two objects is determined by the distance range over which we detect them (see Table 3).

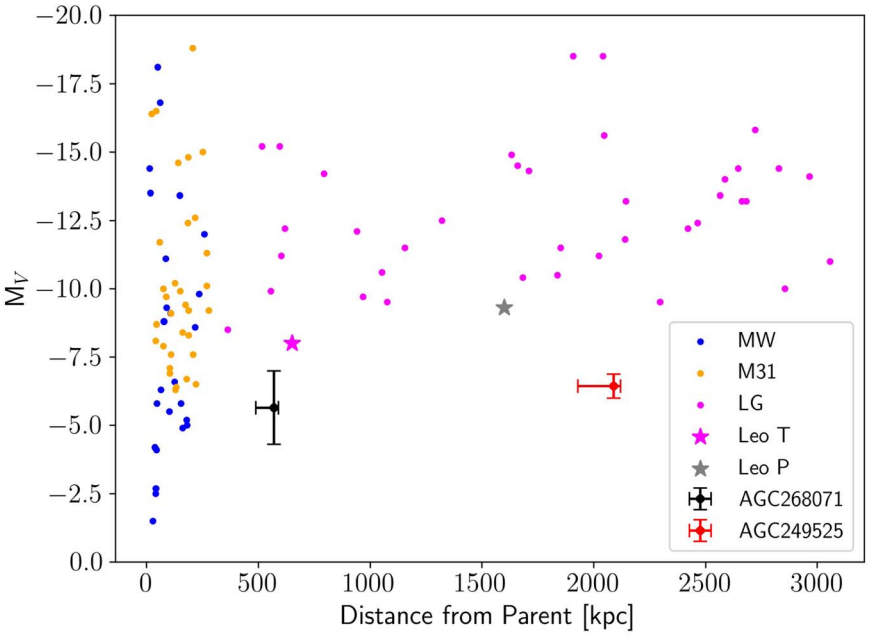

Figure 10. A plot of dwarf galaxy M_V values, drawn from McConnachie (2012), as a function of distance from the parent galaxy for galaxies in and near the Local Group. Milky Way satellite galaxies are plotted in blue while M31 satellites are shown in orange. Dwarf galaxies that are not satellites of either the Milky Way or M31 appear in pink, including Leo T (pink filled star symbol). For the latter set of objects, we plot the distance to the barycenter of the Local Group. Leo P is marked with a filled gray star and plotted using the distance from McQuinn et al. (2015). We also show our measurements for the dwarf galaxy candidate associated with AGC 268071 and AGC 249525 (black and red points with large error bars). For the two dwarf galaxy candidates, we plot the average of the bright and faint absolute magnitude estimates and use both estimates to set the uncertainty. The distance uncertainty is defined by the distance range over which we detect the stellar overdensity. We also note that the distances we are plotting for these two objects are the heliocentric distances.

heliocentric distance determined from our detection and analysis process.

Our estimate of the absolute *V*-band magnitude of the dwarf galaxy candidate associated with AGC 268071 falls toward the faint end of the range of absolute magnitudes for Milky Way satellites and at the very bottom end of the range of luminosities of M31 satellites. The main difference between the AGC 268071 dwarf galaxy candidate and the known satellites of the Milky Way and M31 is its large distance from the Milky Way (which we estimate at ∼570 kpc). This distance

places it substantially farther from the Milky Way or from M31 than any of the other dwarf satellite galaxies that appear on the plot. This suggests that it may not be a satellite of the Milky Way, but may instead be simply a Local Group dwarf galaxy (if it is a genuine galaxy at all); in that case, the most relevant comparison sample for this object would be the other nearby dwarf galaxies that are not satellites (pink points with distances extending to ∼3 Mpc in Figure 10). Compared to this sample of objects, the dwarf galaxy candidate associated with AGC 268071 is roughly 2 mag less luminous, and is also closer in distance than all but a few of the dwarf galaxies in the figure. Overall it seems that the detection for AGC 268071 makes a reasonable dwarf galaxy candidate in the sense that it at least lies within a similar parameter space as the other dwarf galaxies in and around the Local Group, although on the low-luminosity edge of the distribution.

The estimated M_V magnitude and distance for the dwarf galaxy candidate associated with AGC 249525 puts this galaxy ∼2.5 mag below that same sample of nearby dwarf galaxies. This object would thus be a gas-rich ultra-faint dwarf galaxy that is substantially fainter than the other currently known galaxies at this distance (∼2 Mpc). As noted in Janesh et al. (2017), a potential close neighbor to AGC 249525 in terms of distance and sky position is UGC 9128, which is 10° away on the sky and has a heliocentric velocity cz of 152 km s^{-1}(McConnachie 2012), compared to 48 km s^{-1} for AGC 249525.

6.3. Next Steps and Future Observing Capabilities

In our analysis of the ALFALFA UCHVCs, we found six possible dwarf galaxy candidates. However, we again note that —even with our deep optical multiband imaging data, with typical seeing ∼1″ or better— there was no clearly visible diffuse optical emission, nor any obvious (to the eye) stellar association, at the locations of the dwarf galaxy candidates detected via the CMD filtering process. Without such additional evidence, it is appropriate to question whether the objects we found are indeed genuine dwarf galaxies. The statistically significant stellar overdensities we have detected may actually be made up of some combination of compact background galaxies and Galactic foreground stars (that are below the detection limits for Gaia EDR3 and/or SDSS and therefore too faint to be eliminated in the cross-matching step), which happen to coincide with the rough location of the H I source. To confirm that the stars in the detected overdensities are truly associated with the corresponding UCHVC, we would need spectroscopic follow-up observations that show that the stars' velocities are similar to that of the H I. The brightest stars that make up the detections in our best two candidates, AGC 268071 and AGC 249525, have i magnitudes of 20.4 and 23.1 mag, respectively. Deriving accurate radial velocities of stars of these magnitude, even with time on an ∼8−10 m telescope, is challenging; for example, our initial attempt to obtain a spectrum of a star in the AGC 268071 dwarf galaxy candidate using the LRS2 instrument (Chonis et al. 2016) on the 10 m Hobby–Eberly Telescope[12] yielded a spectrum with insufficient signal-to-noise to measure a radial velocity. The rest of the stars that make up the overdensities for our two best candidates are even fainter (see Figures 6 and 7). Thus, follow-up spectroscopy is extremely challenging with current ground-based optical spectroscopy capabilities.

More generally, further progress toward completing the census of low-mass galaxies in the Local Group and its environs will be made with the advent of the next generation of large-scale systematic surveys like the Rubin Observatory's Legacy Survey of Space and Time (LSST; Ivezić et al. 2019). LSST will uniformly survey the Southern sky in six filters (*ugrizy*) over the course of 10 yr; the median 5σ point-source detection limit should be $r = 24$ mag in the single-visit images and r ∼27 mag in the 10 yr coadded images, with median effective seeing of 1.″0. With this wide-field, multicolor, high-quality imaging data, LSST should be able to resolve RGB stars out to ∼10 Mpc within its survey area. The survey should be sensitive to galaxies as faint as the candidate dwarf galaxy we detected in the AGC 268071 field (i.e., M_V ∼−6) in galaxy groups out to ∼3−4 Mpc (LSST Science Collaboration et al. 2009; Simon 2019). LSST should also be able to probe even fainter galaxies with resolved stellar photometry out to 1−2 Mpc and should be complete for galaxies with stellar luminosities $\gtrsim$2–10^3 $L_\odot$ that are within ∼1 Mpc of the Milky Way (Bullock & Boylan-Kolchin 2017). Comparing the catalogs of resolved stars and newly discovered dwarf galaxies that will likely be detected by LSST to H I observations from sensitive radio facilities like the Five Hundred Meter Spherical Telescope, the MeerKAT telescope, the ASKAP telescope, and the planned Square Kilometre Array Observatory may help reveal the nature of objects like the UCHVCs or the Galaxy candidates identified in GALFA-HI data by Saul et al. (2012) and whether these are genuine gas-rich ultra-faint dwarf galaxies or simply isolated gas clouds with no associated stellar population.

Acknowledgments

The authors wish to thank the anonymous referee for providing helpful suggestions that improved the manuscript. We also thank the staff of the WIYN Observatory and Kitt Peak National Observatory for their assistance during our pODI and ODI observing runs. We acknowledge the work of the ALFALFA collaboration in observing, processing, and extracting H I sources. We are grateful to the staff members at WIYN, NOIRLab, and Indiana University Pervasive Technology Institute for designing and implementing the ODI Pipeline, Portal, and Archive (ODI-PPA) and assisting us with the pODI and ODI image reduction. K.L.R., N.J.S., and W.F.J. were supported by NSF grant AST-1615483. J.M.C. is supported by NSF grant AST-2009894. We thank the Indiana University (IU) College of Arts and Sciences for funding IU's share of the WIYN telescope. This research has made use of the NASA/IPAC Extragalactic Database (NED), which is funded by the National Aeronautics and Space Administration and operated by the California Institute of Technology.

Facilities: WIYN (pODI and ODI), Arecibo (ALFA), WSRT .

Software: ODI-PPA (Gopu et al. 2014), QuickReduce pipeline (Kotulla 2014), IRAF (Tody 1986, 1993), Python (https://www.python.org), Astropy (Astropy Collaboration et al. 2013, 2018, 2022).

[12] Based on observations obtained with the Hobby–Eberly Telescope (HET), which is a joint project of the University of Texas at Austin, the Pennsylvania State University, Ludwig-Maximillians-Universitaet Muenchen, and Georg-August Universitaet Goettingen. The HET is named in honor of its principal benefactors, William P. Hobby and Robert E. Eberly.

ORCID iDs

Katherine L. Rhode https://orcid.org/0000-0001-8283-4591
Nicholas J. Smith https://orcid.org/0000-0002-3222-2949
William F. Janesh https://orcid.org/0000-0003-4364-0799
John J. Salzer https://orcid.org/0000-0001-8483-603X
Elizabeth A. K. Adams https://orcid.org/0000-0002-9798-5111
Martha P. Haynes https://orcid.org/0000-0001-5334-5166
Steven Janowiecki https://orcid.org/0000-0001-9165-8905
John M. Cannon https://orcid.org/0000-0002-1821-7019

References

Adams, E. A. K., Giovanelli, R., & Haynes, M. P. 2013, ApJ, 768, 77
Adams, E. A. K., Cannon, J. M., Rhode, K. L., et al. 2015, A&A, 580, A134
Adams, E. A. K., Oosterloo, T. A., Cannon, J. M., Giovanelli, R., & Haynes, M. P. 2016, A&A, 596, A117
Applebaum, E., Brooks, A. M., Christensen, C. R., et al. 2021, ApJ, 906, 96
Astropy Collaboration, Price-Whelan, A. M., Lim, P. L., et al. 2022, ApJ, 935, 167
Astropy Collaboration, Price-Whelan, A. M., Sipőcz, B. M., et al. 2018, AJ, 156, 123
Astropy Collaboration, Robitaille, T. P., Tollerud, E., et al. 2013, A&A, 558, A33
Baumgardt, H., & Hilker, M. 2018, MNRAS, 478, 1520
Bell, E. F., McIntosh, D. H., Katz, N., & Weinberg, M. D. 2003, ApJS, 149, 289
Bellazzini, M., Beccari, G., Battaglia, G., et al. 2015a, A&A, 575, A126
Bellazzini, M., Magrini, L., Mucciarelli, A., et al. 2015b, ApJL, 800, L15
Bennet, P., Sand, D. J., Crnojević, D., et al. 2022, ApJ, 924, 98
Birkinshaw, M., Ho, P. T. P., & Baud, B. 1983, A&A, 125, 271
Bralts-Kelly, L., Paine, S., Adams, E. A., et al. 2020, BAAS, 52, 168.01
Bullock, J. S., & Boylan-Kolchin, M. 2017, ARA&A, 55, 343
Chambers, K. C., Magnier, E. A., Metcalfe, N., et al. 2016, arXiv:1612.05560
Chonis, T. S., Hill, G. J., Lee, H., et al. 2016, Proc. SPIE, 9908, 99084C
DeFelippis, D., Putman, M., & Tollerud, E. 2019, ApJ, 879, 22
Dehnen, W., McLaughlin, D. E., & Sachania, J. 2006, MNRAS, 369, 1688
Eisenstein, D. J., Weinberg, D. H., Agol, E., et al. 2011, AJ, 142, 72
Erkes, J. W., & Philip, A. G. D. 1975, ApJ, 197, 533
Evans, C. J., Castro, N., Gonzalez, O. A., et al. 2019, A&A, 622, A129
Faulkner, D. J., Scott, T. R., Wood, P. R., & Wright, A. E. 1991, ApJL, 374, L45
Frank, J., & Gisler, G. 1976, MNRAS, 176, 533
Freire, P. C., Kramer, M., Lyne, A. G., et al. 2001, ApJL, 557, L105
Gaia Collaboration, Brown, A. G. A., Vallenari, A., et al. 2021, A&A, 649, A1
Gaia Collaboration, Prusti, T., de Bruijne, J. H. J., et al. 2016, A&A, 595, A1
Garrison-Kimmel, S., Boylan-Kolchin, M., Bullock, J. S., & Lee, K. 2014, MNRAS, 438, 2578
Giovanelli, R., Haynes, M. P., Adams, E. A. K., et al. 2013, AJ, 146, 15
Giovanelli, R., Haynes, M. P., Kent, B. R., et al. 2005, AJ, 130, 2598
Giovanelli, R., Haynes, M. P., Kent, B. R., & Adams, E. A. K. 2010, ApJL, 708, L22
Girardi, L., Grebel, E. K., Odenkirchen, M., & Chiosi, C. 2004, A&A, 422, 205
Gopu, A., Hayashi, S., Young, M. D., et al. 2014, Proc. SPIE, 9152, 91520E
Grogin, N. A., Kocevski, D. D., Faber, S. M., et al. 2011, ApJS, 197, 35
Harris, W. E. 1996, AJ, 112, 1487
Haynes, M. P., Giovanelli, R., Kent, B. R., et al. 2018, ApJ, 861, 49
Haynes, M. P., Giovanelli, R., Martin, A. M., et al. 2011, AJ, 142, 170
Heiles, C., & Henry, R. C. 1966, ApJ, 146, 953
Hilker, M. 2006, A&A, 448, 171
Irwin, M. J., Belokurov, V., Evans, N. W., et al. 2007, ApJL, 656, L13
Janesh, W., Rhode, K. L., Salzer, J. J., et al. 2015, ApJ, 811, 35
Janesh, W., Rhode, K. L., Salzer, J. J., et al. 2017, ApJL, 837, L16
Janesh, W., Rhode, K. L., Salzer, J. J., et al. 2019, AJ, 157, 183
Janesh, W. F. 2018, PhD Thesis, Indiana Univ. Bloomington
Jester, S., Schneider, D. P., Richards, G. T., et al. 2005, AJ, 130, 873
Ivezić, Ž., Kahn, S. M., Tyson, J. A., et al. 2019, ApJ, 873, 111
Kerr, F. J., & Knapp, G. R. 1972, AJ, 77, 573
Knapp, G. R., Rose, W. K., & Kerr, F. J. 1973, ApJ, 186, 831
Koch, A., Côté, P., & McWilliam, A. 2009, A&A, 506, 729
Koekemoer, A. M., Faber, S. M., Ferguson, H. C., et al. 2011, ApJS, 197, 36
Kotulla, R. 2014, in ASP Conf. Ser. 485, Astronomical Data Analysis Software and Systems XXIII, ed. N. Manset & P. Forshay (San Francisco, CA: ASP), 375
LSST Science Collaboration, Abell, P. A., Allison, J., et al. 2009, arXiv:0912.0201
McConnachie, A. W. 2012, AJ, 144, 4
McQuinn, K. B. W., Skillman, E. D., Dolphin, A., et al. 2015, ApJ, 812, 158
Paine, S., Bralts-Kelly, L., Adams, E., et al. 2020, BAAS, 52, 168.02
Palma, C., Majewski, S. R., & Johnston, K. V. 2002, ApJ, 564, 736
Peek, J. E. G., Heiles, C., Douglas, K. A., et al. 2011, ApJS, 194, 20
Rhode, K. L., Salzer, J. J., Haurberg, N. C., et al. 2013, AJ, 145, 149
Roberts, M. S. 1959, Natur, 184, 1555
Roberts, M. S. 1960, AJ, 65, 457
Ryan-Weber, E. V., Begum, A., Oosterloo, T., et al. 2008, MNRAS, 384, 535
Sand, D. J., Crnojević, D., Bennet, P., et al. 2015, ApJ, 806, 95
Sand, D. J., Seth, A. C., Crnojević, D., et al. 2017, ApJ, 843, 134
Saul, D. R., Peek, J. E. G., Grcevich, J., et al. 2012, ApJ, 758, 44
Schlafly, E. F., & Finkbeiner, D. P. 2011, ApJ, 737, 103
Schlegel, D. J., Finkbeiner, D. P., & Davis, M. 1998, ApJ, 500, 525
Sharina, M. E., Ryabova, M. V., Maricheva, M. I., & Gorban, A. S. 2018, ARep, 62, 733
Simon, J. D. 2019, ARA&A, 57, 375
Skillman, E. D., Salzer, J. J., Berg, D. A., et al. 2013, AJ, 146, 3
Smith, N. J. 2022, PhD thesis, Indiana Univ. Bloomington
Spergel, D. N. 1991, Natur, 352, 221
Stefanon, M., Yan, H., Mobasher, B., et al. 2017, ApJS, 229, 32
Tody, D. 1986, Proc. SPIE, 627, 733
Tody, D. 1993, in ASP Conf. Ser. 52, Astronomical Data Analysis Software and Systems II, ed. R. J. Hanisch, R. J. V. Brissenden, & J. Barnes (San Francisco, CA: ASP), 173
Tollerud, E. J., Geha, M. C., Grcevich, J., et al. 2016, ApJ, 827, 89
Tollerud, E. J., Geha, M. C., Grcevich, J., Putman, M. E., & Stern, D. 2015, ApJL, 798, L21
Tollerud, E. J., & Peek, J. E. G. 2018, ApJ, 857, 45
van den Bergh, S. 2010, AJ, 140, 1043
van Loon, J. T., Stanimirović, S., Evans, A., & Muller, E. 2006, MNRAS, 365, 1277
van Loon, J. T., Stanimirović, S., Putman, M. E., et al. 2009, MNRAS, 396, 1096
Walsh, S. M., Willman, B., & Jerjen, H. 2009, AJ, 137, 450
York, D. G., Adelman, J., Anderson, J. E. J., et al. 2000, AJ, 120, 1579
Young, M. D., Kotulla, R., & Gopu, A. 2014, Proc. SPIE, 9152, 91522U